

# A Revised Oceanic Plate Cooling Model

M.C.Holdt<sup>1</sup>, N.J.White<sup>1</sup> and F.D. Richards<sup>2</sup>

<sup>1</sup>Bullard Laboratories, Department of Earth Sciences, University of Cambridge, Madingley Rise,  
Madingley Road, Cambridge, CB3 0EZ, UK

<sup>2</sup>Department of Earth Sciences and Engineering, Imperial College London, Prince Consort Road, South  
Kensington, London, SW7 2BP, UK

## Key Points:

- Global age-depth ( $n = 10,863$ ) and heat flow ( $n = 3,573$ ) measurements are used to reassess different oceanic plate cooling models.
- Simple and comprehensive parameterizations yield similar estimates of equilibrium plate thickness and temperature.
- Thickness of seismogenic layer determined by depth to 700°C isothermal surface.

13 **Abstract**

14 Global age-depth and heat flow observations provide constraints for cooling and subsi-  
 15 dence of oceanic plates. Numerous studies have addressed this problem, which has a bear-  
 16 ing upon the calibration of shear-wave tomographic models and upon lithospheric rhe-  
 17 ology. The robustness of these results depends upon the quality and spatial distribution  
 18 of both age-depth and heat flow measurements. Here, we revisit the plate cooling model  
 19 for two reasons. First, a database of 10,863 age-depth measurements that are distributed  
 20 throughout the oceanic realm has been constructed. This database is combined with 3,573  
 21 heat flow measurements. Secondly, we wish to explore a range of analytical and numer-  
 22 ical plate models that incorporate the temperature- and pressure-dependence of conduc-  
 23 tivity, of expansivity, and of specific heat capacity. Our goal is to identify plate models  
 24 that jointly fit observational constraints, whilst honoring laboratory-based constraints  
 25 for the values of key thermal parameters. Both simple analytical and comprehensive  
 26 numerical parameterizations recover an equilibrium plate thickness of  $105 \pm 10$  km or  $96 \pm$   
 27 10 km with a temperature of  $1326 \pm 50^\circ\text{C}$ . This recovered temperature is consistent with  
 28 independent petrologic constraints. Spatial analysis of age-depth measurements demon-  
 29 strates that previously invoked transient plate shallowing is not globally observed. This  
 30 observation implies that the possible onset of a convective instability, which has been pro-  
 31 posed as a mechanism to stabilize equilibrium plate thickness, might act on shorter length  
 32 scales than that implied by previously reported transient shallowing. Finally, our revised  
 33 plate model is used to track lithospheric thermal structure as a function of time and to  
 34 calculate residual depth anomalies.

35 **Plain Language Summary**

36 Earth's outermost layer, known as the lithosphere, comprises several interlocking  
 37 tectonic plates. Throughout the oceans, seafloor is continuously created at mid-oceanic  
 38 ridges, which are associated with high temperatures. When the new seafloor moves away  
 39 from the mid-oceanic ridge, it gradually cools and sinks over many millions of years. Al-  
 40 though this interesting problem has been studied by many scientists, it is always insight-  
 41 ful to revisit it using modern measurements. Here, we use a newly assembled set of global  
 42 depth and temperature measurements to revise the plate cooling model. Our results show  
 43 that excellent fits to measurements can be achieved with both simple and comprehen-  
 44 sive parameterizations. The plate model can be used to improve our understanding of  
 45 the thermal structure of the Earth. It is also an essential starting point for calculating  
 46 vertical deflection of the Earth's surface caused by the stirring of hot material that lies  
 47 beneath the plates.

48 **1 Introduction**

49 It is generally accepted that oceanic lithosphere cools and subsides as a function  
 50 of plate age (McKenzie, 1967; Turcotte & Oxburgh, 1967). This phenomenon is man-  
 51 ifest by a combination of both age-depth and heat flow observations from the oceanic  
 52 realm. Since the late 1960s, two principal classes of models have been developed to ac-  
 53 count for the evolution of oceanic lithosphere. Early studies suggested that a half-space  
 54 cooling model accounts for age-depth observations (Takeuchi & Sakata, 1970; Davis &  
 55 Lister, 1974). In this model, subsidence and heat flow are functions of the square root  
 56 of crustal age. The half-space cooling model is based upon observations from relatively  
 57 young (i.e.  $<80$  Ma) oceanic crust and implicitly assumes that cooling and subsidence  
 58 continue indefinitely with time. The observational database expanded when studies of  
 59 oceanic magnetic anomalies enabled ages of subsidence anomalies on older oceanic crust  
 60 to be dated (Vogt et al., 1971; Larson & Hilde, 1975; Hilde et al., 1976). Subsequently,  
 61 Parsons and Sclater (1977) analyzed measurements from oceanic crust as old as 163 Ma  
 62 and observed that the depth of seafloor that is older than  $\sim 80$  Ma is shallower than

that predicted by the half-space cooling model. They proposed that the plate model of McKenzie (1967), where temperature along a basal boundary of the cooling lithosphere is fixed to simulate resupply of heat, yields a better fit to a combination of age-depth and heat flow measurements. Stein and Stein (1992) built upon this pioneering analysis by jointly inverting an extensive database of age-depth and heat flow measurements from the North Pacific Ocean and from the northwest Atlantic Ocean. It is now generally accepted that the plate model, rather than the half-space cooling model, provides a better description of the subsidence and heat flow characteristics of oceanic lithosphere. A significant drawback of the half-space cooling model is its inability to adequately fit age-depth and heat flow observations using a basal temperature that is consistent with independent petrologic and geochemical constraints (Hoggard et al., 2017).

In recent years, there has been considerable interest in developing and applying more physically realistic plate models that include, for example, temperature- and pressure-dependence of thermal parameters. McKenzie et al. (2005) showed that the thermal structure of the lithosphere can be constrained by using experimentally determined values of thermal conductivity,  $k$ , of thermal expansivity,  $\alpha$ , and of specific heat capacity,  $C_p$ . Subsequent models have incorporated more physically accurate parameterizations, which include lithostatic pressure gradients, revised estimates of the radiative component of thermal conductivity, mineral phase transitions, hydrothermal circulation as well as an insulating crustal layer (Afonso et al., 2007; Grose & Afonso, 2013; T. Korenaga & Korenaga, 2016; Richards et al., 2018). Notwithstanding these developments, the success of a lithospheric thermal model still depends upon the ability to match a combination of age-depth and heat flow measurements. When jointly inverting these measurements, the robustness of an optimal model is predicated upon their quality and spatial distribution. A global database of age-depth observations assembled by Holdt et al. (2022) presents an opportunity to reassess the range of analytical and numerical plate models that have been proposed. It is important to acknowledge that the plate model is not universally accepted and that alternative oceanic cooling models have been proposed (Davies, 1988; Doin & Fleitout, 1996; Huang & Zhong, 2005; J. Korenaga, 2015; T. Korenaga et al., 2021).

Plate models typically recover values of temperature,  $T$ , lithospheric thickness,  $z_p$ , and in some cases ridge depth,  $z_r$ . For analytical models,  $T$  is defined as the temperature along the basal boundary of the lithosphere,  $T_b$ . In contrast, numerical models have a more flexible parameterization, which can be used to design more physically realistic temperature structures at and away from boundaries. In these schemes, which account for the isentropic temperature gradient of the convecting mantle, it is important to note that  $T$  refers to average potential temperature,  $T_p$ , not actual basal temperature (McKenzie & Bickle, 1988).  $z_p$  is the base of the oceanic lithosphere which is defined to consist of the mechanical boundary layer and part of the thermal boundary in accordance with McKenzie and Bickle (1988). It can also be regarded as an isothermal surface (see Priestley and McKenzie (2013)). Finally,  $z_r$  is defined as the global average depth of the mid-oceanic ridge axes that is isostatically corrected for sedimentary load and variable crustal thickness. Since there are independent constraints for these three parameters, the values recovered for the optimal plate model are testable.

The aims of this contribution are threefold. First, we test a variety of plate models by jointly inverting global databases of age-depth and heat flow measurements constructed by Holdt et al. (2022) and by Hasterok et al. (2011), respectively (Figure 1). These plate models include two simple analytical plate models and a more physically realistic temperature- and pressure-dependent parameterization. Our goal is to identify simple plate models that yield the best fit to observational constraints whilst also honoring independent petrologic and mineral physical constraints. Note that we specifically confine our attention to plate models and do not discuss alternative possibilities (e.g. T. Korenaga et al. (2021)). Secondly, we show that the transient shallowing for plate ages of

80–130 Ma that was observed by Crosby et al. (2006) and by several older studies is principally caused by an extensive plate-scale age-depth anomaly. Many positive and negative age-depth anomalies occur globally, which Holdt et al. (2022) and many previous authors have interpreted as the signal of mantle dynamic topography that is generated and maintained by convective processes. This observation highlights the importance of exploiting global age-depth and heat flow databases, which have improved spatial coverage. Finally, we use our results to infer possible scaling characteristics of the convective instability, whose existence has been invoked to stabilize plate thickness (Parsons & McKenzie, 1978). We conclude by revising the rheological properties of oceanic lithosphere that can be determined from the thermal structure calculated from plate models.

## 2 Observational Constraints

### 2.1 Age-Depth Measurements

Age-depth observations are a primary constraint for the plate and other models since they determine how oceanic lithosphere subsides as a function of time as a result of cooling and thickening. Here, we exploit a global database of water-loaded measurements of the depth to oceanic basement that was compiled by Holdt et al. (2022). This database contains 10,863 measurements and represents the largest compilation of accurately determined water-loaded estimates obtained from a combination of modern/legacy seismic reflection profiles and wide-angle experiments (Figure 1a). A combination of academic and commercial surveys was exploited. We note that Holdt et al. (2022) used the same global database to identify and measure the amplitudes and wavelengths of regional age-depth anomalies on many different spatial scales throughout the oceanic realm. They argue, along with many previous authors, that these anomalies can be regarded as a proxy for mantle dynamic topography. Here, our aims are different but related—we wish to use these age-depth observations together with global heatflow measurements to re-examine cooling and thickening of oceanic lithosphere. Although this problem has been exhaustively studied, we believe that our new global database can shed new and helpful insights.

Water-loaded depth to oceanic basement,  $w$ , is calculated as accurately as possible by carrying out two well-known corrections. The sedimentary correction,  $C_s$ , converts the variable thickness and density of the sedimentary load into an equivalent water load using the scheme described in detail by Hoggard et al. (2017) and subsequently revised by Holdt et al. (2022). The crustal correction,  $C_c$ , converts variable thickness and density of oceanic crust into a standard crustal reference column. The corrected depth to oceanic basement is given by  $w = z_{sb} + C_s + C_c$  where  $z_{sb}$  is bathymetry. It is important to emphasize that  $C_s$  is generally more significant than  $C_c$ . From a global perspective,  $C_s$  is accurately determinable since  $\sim 70\%$  of locations have sedimentary columns that are  $\leq 0.5$  km. Where crustal thickness and density are unknown, the value of  $C_c$  is gauged from regional crustal information, which yields either an upper or a lower bound for  $w$ . Table 1 lists the symbols and values of all parameters used within this study.

The database constructed by Holdt et al. (2022) represents a significant improvement in terms of both the quantity and the spatial distribution of accurate age-depth measurements. Previously constructed databases are often of only regional extent (see, e.g., Parsons and Sclater (1977); Stein and Stein (1992)), rely upon gridded values whose accuracy is difficult to gauge (see, e.g., Crosby et al. (2006); Crosby and McKenzie (2009)), or are spatially biased toward continental margins (see, e.g., Richards et al. (2018)). The revised and augmented database builds upon the detailed approach taken by Hoggard et al. (2017), primarily by interpreting substantial quantities of modern multi-channel and legacy single-channel seismic reflection profiles that criss-cross oceanic lithosphere of different ages. The inclusion of additional profiles dramatically improves spatial coverage throughout the oceanic realm. Age-depth measurements are always carried out on

*bona fide* oceanic crust located away from anomalous tectonic features (e.g. seamounts, fracture zones, flexural moats). To aid spatial clarity, detailed measurements along individual profiles are binned every  $1^\circ$ . They are also assigned ages using a modern magnetic age grid (Seton et al. (2020); Figure 1c).

Figure 2a presents 10,863 age-depth measurements as a function of oceanic plate age. Note that more uncertain age-depth measurements from oceanic crust that is older than 200 Ma are omitted. This cloud of measurements has two significant characteristics. First, a mean relationship is evident, whereby subsidence increases exponentially from  $\sim 2.5$  km to  $\sim 6$  km as a function of plate age. Secondly, there is considerable but relatively uniform scatter about this mean relationship. The envelope of scatter is consistently  $\pm 1$  km, regardless of plate age. Since the pioneering work of Menard (1973), it is generally accepted that age-depth measurements that lie above or below the mean relationship represent positive and negative residual depth anomalies, respectively. These anomalies are interpreted as maximum signals of dynamic topography generated by mantle convective processes. For comparative purposes, Figure 2b shows these age-depth measurements binned every 2.5 Ma.

Previous plate model studies have sometimes attempted to minimize the influence of dynamic topography by excising regions dominated by dynamic topographic anomalies. For example, Crosby et al. (2006) exploited age-depth observations from regions, which featured near-zero (or at least minimal) gravity anomalies in order to avoid significant dynamic upwelling and downwelling. Goutorbe and Hillier (2013) removed age-depth measurements within the vicinity of major mantle plumes. Subsequently, Hoggarde et al. (2016) used a global database of age-depth measurements which demonstrated that residual depth anomalies are ubiquitous down to wavelengths as short as 1000 km. Here, we have not applied any such spatial filters. Instead, we assume that our database of 10,863 measurements represents a uniformly dense sampling of the oceanic realm so that dynamic upwellings and downwellings are potentially equally included over a complete range of plate ages (Holdt et al., 2022).

## 2.2 Heat Flow Measurements

Heat flow observations, which enable conductive heat loss through the surface of the lithospheric plate to be determined as a function of time, also help to constrain plate cooling. In the oceanic realm, standard heat flow measurements are acquired using a probe that is inserted into the sedimentary pile which measures temperature gradient and the *in situ* thermal conductivity (Slater et al., 2014). Heat flow,  $H$ , is given by  $H = k(\Delta T/\Delta z)$ , where  $k$  is thermal conductivity, and  $\Delta T/\Delta z$  is the thermal gradient between two points. A comprehensive global compilation of 23,428 heat flow observations was carefully compiled by Hasterok et al. (2011). This substantial undertaking provides an excellent complementary constraint for plate model considerations (Figure 1b).

Following the detailed methodology outlined by Hasterok et al. (2011) and by Richards et al. (2018), heat flow measurements are filtered and corrected. First, observations are edited by removing points which do not lie upon *bona fide* oceanic crust identified by a combination of linear magnetic anomalies and tripartite seismic structure, by deleting negative values and by binning the data at intervals of  $0.1^\circ$  to reduce the spatial bias associated with densely sampled locations. Secondly, measurements are excised if they lie between 0 and 65 Ma and have sedimentary thicknesses of less than 0.4 km. This filtering step is the most significant one since it excludes the majority of measurements from young oceanic crust. Although this filtering strategy reduces the number of measurements between 0 and 65 Ma, it is essential to isolate and remove any measurements that could be significantly perturbed by hydrothermal circulation, which primarily affects young oceanic crust (Hasterok, 2013; Stein & Stein, 1992). For this specific purpose, sedimentary thicknesses are taken from the GlobSed global grid (Straume et al., 2019). Thirdly,

measurements are excised if they are within 60 km of seamounts or igneous plateaux. Locations of seamounts and large igneous provinces are taken from Wessel et al. (2010) and from Coffin and Eldholm (1994), respectively. Heat flow measurements from oceanic crust that is older than 200 Ma are omitted on two grounds. First, there are only  $\sim 10$  measurements on oceanic crust beyond 200 Ma. Secondly, their values lie below the average value of  $0.05 \text{ W m}^{-2}$  at old plate ages. Finally, a sedimentation correction is applied in order to account for depression of the geothermal profile caused by rapid deposition. Reduced heat flow occurs since the initial temperature of uncompacted sediment is equal to that of bottom water. Assuming that the rate of sedimentation and the value of thermal diffusivity are constant as a function of time, Von Herzen and Uyeda (1963) calculated the fractional perturbation of the geothermal profile at the seabed,  $F$ , in the absence of internal heat generation. A simplified version of the analytical solution is given by

$$F = 1 + 2Y^2 \operatorname{erfc}(Y) - \operatorname{erf}(Y) - \frac{2Y}{\sqrt{\pi}} \exp(-Y^2), \quad (1)$$

where  $Y = \frac{1}{2}U t_s^{\frac{1}{2}} \kappa_s^{-\frac{1}{2}}$ ,  $U$  is the rate of sedimentation,  $t_s$  is the duration of sedimentation, and  $\kappa_s$  is thermal diffusivity of the sedimentary pile. Following Hasterok et al. (2011) and Richards et al. (2018),  $U$  is estimated by dividing sedimentary thickness by  $t_s$ , which is assumed to be equal to plate age. The impact of the sedimentation correction is relatively small. For example, 76% of measurements are corrected by  $\leq 10\%$ , when  $\kappa_s$  is assumed to be  $0.25 \text{ mm}^2 \text{ s}^{-1}$ . Following Richards et al. (2018), measurements from certain anomalous regions (e.g. Caspian Sea, Gulf of Mexico, Black Sea) are omitted because  $U$  significantly increased in these regions during Miocene times, violating the assumption of constant sedimentation rate (Knapp et al., 2007; Galloway et al., 2011; Sydorenko et al., 2017).

The application of this filtering and editing process yields a set of 3,573 heat flow measurements. Figure 2c presents corrected heat flow measurements as a function of oceanic plate age. Although there is considerable and variable scatter, a clear average relationship is visible. The average heat flow at mid-oceanic ridges is  $\sim 0.25 \text{ W m}^{-2}$  and decreases exponentially to a value of  $\sim 0.05 \text{ W m}^{-2}$  for the oldest oceanic lithosphere. For comparative purposes, these measurements have also been binned every 2.5 Ma (Figure 2d).

### 3 Modeling Strategy

The first detailed application of a plate model to age-depth and heat flow observations was carried out by Parsons and Sclater (1977) who derived appropriate partial differential equations, developed analytical solutions, and matched theory with observation. Their primary focus concerned fitting of age-depth observations from the North Pacific and North Atlantic oceans. They separately showed that their optimal plate model also matched limited heat flow observations. Subsequently, Stein and Stein (1992) employed a very similar analytical approach to jointly invert age-depth and heat flow observations. In both publications, the primary focus is recovery of basal temperature and equilibrium plate thickness. The critical underpinning thermal parameters are thermal conductivity,  $k$ , thermal expansivity,  $\alpha$ , and isobaric specific heat capacity,  $C_p$ . Analytical solutions can be derived if these three parameters are assumed to be constant.

McKenzie et al. (2005) developed a more physically realistic version of the original plate model, which accounts for the temperature dependence of  $k$ ,  $\alpha$  and  $C_p$ , as well as isentropic decompression and melting of the mantle beneath the mid-ocean ridge in its initial temperature condition. This elaboration was motivated by the results of laboratory experiments, which clearly demonstrate that the values of these thermal parameters vary significantly over the temperature and pressure ranges observed within an olivine-

dominated lithospheric mantle (Berman & Aranovich, 1997; Bouhifd et al., 1996; Hofmeister, 2010). Subsequent plate models have become increasingly sophisticated and, in general, are numerically solved in the absence of easily derived analytical solutions (Grose & Afonso, 2013; T. Korenaga & Korenaga, 2016; Richards et al., 2018).

Thermal evolution of oceanic lithosphere is calculated by solving the one-dimensional heat equation in a horizontally translating reference frame, reflecting the movement of the lithosphere away from the ridge axis. The general form of this equation is given by

$$\rho(T, P, X) C_p(T, X) \frac{\partial T}{\partial t} = \frac{\partial}{\partial z} \left[ k(T, P, X) \frac{\partial T}{\partial z} \right], \quad (2)$$

where  $z$  is depth,  $t$  is time, and  $\rho$  is density,  $T$  is temperature,  $P$  is pressure and  $X$  is composition. In Equation (2),  $k$  and  $\rho$  depend upon  $T$ ,  $P$ , and  $X$ .  $C_p$  primarily depends upon  $T$  and  $X$  since its pressure dependence is negligible over the range of pressures encountered within the lithosphere (Hofmeister, 2007).

If  $k$ ,  $\alpha$  and  $C_p$  are assumed to be constant, analytical solutions for subsidence and heat flow can be derived using standard Fourier expansion (Carslaw & Jaeger, 1959). Subsidence as a function of time,  $w(t)$ , is given by

$$w(t) = z_r + \frac{\rho_m \alpha (T - T_0) z_p}{2(\rho_m - \rho_w)} \left[ 1 - \frac{8}{\pi^2} \sum_{i=0}^N \frac{1}{(1+2i)^2} \exp - \frac{\kappa(1+2i)^2 \pi^2 t}{z_p^2} \right], \quad (3)$$

where  $\kappa = k/\rho_m C_p$ ,  $\rho_m$  is density of mantle at  $0^\circ\text{C}$ ,  $\rho_w$  is density of the water column,  $T$  is temperature of the basal boundary at the ridge axis,  $T_0 = 0^\circ\text{C}$  is surface temperature, and  $i$  is an integer whose maximum value is chosen to achieve convergence. Heat flow as a function of time,  $H(t)$ , is given by

$$H(t) = \frac{k(T - T_0)}{z_p} \left[ 1 + 2 \sum_{i=1}^N \exp \frac{-\kappa i^2 \pi^2 t}{z_p^2} \right]. \quad (4)$$

When comparing Equations 3 and 4, it is evident that, for a fixed  $w$ , a higher  $T$  requires a thinner  $z_p$ , and for a fixed  $H$ , a higher  $T$  requires a thicker  $z_p$ . If  $k$ ,  $\alpha$  and  $C_p$  vary as a function of pressure and temperature,  $w(t)$  is calculated by numerically solving

$$w(t) = z_r + \frac{\rho_b}{\rho_m - \rho_w(t)} \int_0^{z_p} \left[ 1 - \frac{\rho(0, z')}{\rho(t, z')} \right] dz', \quad (5)$$

where  $z'$  is the Lagrangian depth co-ordinate that contracts as a result of lithospheric cooling,  $\rho_b$  is density at the depth of compensation which is defined as the depth down to which conductive cooling occurs (i.e. the shallowest depth where  $\rho(t, z') = \rho(0, z')$ ), and  $\rho_w(t) = 1.028 + 0.00424w(t) \text{ Mg m}^{-3}$  to account for compressibility of the water column (Grose & Afonso, 2013).  $\rho_w$  increases as a function of time since the seabed deepens due to lithospheric cooling, which slightly amplifies the thickness of the water column,  $w(t)$ .

Heat flow,  $H(t)$ , is calculated using a finite-difference scheme which solves

$$H(n\Delta t) = \frac{k_0^n (T_1^n - T_0^n)}{\Delta z_0^n}, \quad (6)$$

where  $n$  is an integer,  $\Delta t$  is the time interval between nodes,  $\Delta z_0^n$  is the depth interval between nodes,  $k_0^n$  is surface conductivity,  $T_0^n$  is surface temperature, and  $T_1^n$  is temperature at the next node beneath the surface. In other words,  $H(t)$  is calculated at the upper surface of the plate. Temperature-dependent models adopt parameterisations derived from experimental data on olivine. The temperature and pressure dependence of  $k$ ,  $\alpha$  and  $C_p$  have been determined using a range of different laboratory experiments on olivine, which are summarized in detail by Richards et al. (2020) where the necessary equations are given in their Appendix C ( $k(P, T)$ : Equation (C.6);  $\alpha(P, T)$ : Equation (C.9); and  $C_p$ : Equation (C.4)). Note that there are small but significant differences between the details of our thermal parameterization and those of Richards et al. (2018). For  $k$ , we use the parameterization of Pertermann and Hofmeister (2006) for dunite; for  $\alpha$ , we use the parameterization of Bouhifd et al. (1996) presented in their Figure 3 (i.e.,  $\alpha_0 = 2.368 \times 10^{-5}$  and  $\alpha_1 = 1.108 \times 10^{-8}$ , not the values from their Table 2), and for  $C_p$ , we use the parameterization of Berman and Aranovich (1997), assuming an olivine composition of 89% forsterite and 11% fayalite where  $c_0 = 1611$ ,  $c_1 = 12484$  and  $c_2 = 1729 \times 10^6$ .

The insulating properties of oceanic crust can also be included. We adopt a pressure and temperature-dependent parameterization for  $k$ ,  $\alpha$ , and  $C_p$  for the insulating crustal layer (see Appendix C of Richards et al. (2018), Equations C.11, C.12 and C.13). Following Grose and Afonso (2013) and Richards et al. (2018), a thin insulating crustal layer at the top of the cooling lithospheric plate is simulated by assuming, based upon petrologic analysis of oceanic drill core and mapping of ophiolites, that plagioclase is the dominant crystalline phase throughout the tripartite structure of oceanic crust (Dick et al., 2000; Carlson & Jay Miller, 2004; VanTongeren et al., 2021). Since plagioclase has a thermal conductivity which is  $\sim 25\%$  that of olivine, oceanic crust can have a potentially significant insulating effect upon the underlying lithospheric mantle, provided that heat is transferred by conduction alone. A geometric mean is used to estimate the conductivity of an aggregate that comprises plagioclase, diopside and olivine (Grose & Afonso, 2013). This assumption yields an average crustal conductivity of  $2.65 \text{ W m}^{-1} \text{ K}^{-1}$  which is broadly consistent with the results of deep-sea drilling expeditions (e.g.  $2 \text{ W m}^{-1} \text{ K}^{-1}$ ; Kelemen et al. (2004)).

## 4 Model Assessment and Benchmarking

Sets of subsidence and heat flow calculations are generated by systematically varying three key parameters: mantle temperature,  $T$  (equivalent to basal temperature,  $T_b$ , in our analytical models or potential temperature,  $T_p$ , in our numerical models); lithospheric thickness,  $z_p$ ; and ridge depth,  $z_r$ . Thus,  $T$  is varied between 1100 and 1600°C at increments of 25°C,  $z_p$  is varied between 60 and 160 km at increments of 5 km.  $z_r$  is generally assumed to be  $2.5 \pm 0.3$  km but in some instances its value is varied between 2 and 3 km at increments of 0.05 km. In order to identify those models that yield optimal fits to age-depth and heat flow observations, the root mean squared (rms) misfit is calculated by carrying out parameter sweeps, which interrogate the three-dimensional misfit space. The formal misfit between observed and calculated subsidence,  $\chi_s$ , is given by

$$\chi_s = \sqrt{\frac{1}{N_s} \sum_{i=1}^{N_s} \left( \frac{w_i^o - w_i^c}{\sigma_i} \right)^2}, \quad (7)$$

where  $w_i^o$  and  $w_i^c$  are observed and calculated values of water-loaded subsidence,  $N_s$  is the number of age bins, and  $\sigma_i$  is the interquartile range of each bin. The misfit between observed and calculated heat flow,  $\chi_h$ , is given by

$$\chi_h = \sqrt{\frac{1}{N_h} \sum_{i=1}^{N_h} \left( \frac{H_i^o - H_i^c}{\sigma_i^*} \right)^2}, \quad (8)$$

where  $H_i^o$  and  $H_i^c$  are observed and calculated values of heat flow,  $N_h$  is the number of age bins, and  $\sigma_i^*$  is the interquartile range of each bin. Figure 2a shows that there is a noticeable reduction in the number of age-depth measurements older than 168 Ma, which contributes to a greater degree of uncertainty (Figure 2b). Following Richards et al. (2018), age-depth and heat flow measurements from oceanic crust that is older than 168 Ma are excluded to avoid spatial bias. Furthermore, measurements younger than 5 Ma can be omitted to mitigate the potential influence of hydrothermal circulation at the ridge axis (Grose & Afonso, 2013).

Following Stein and Stein (1992), we also interrogate the joint misfit between observed and calculated values of subsidence and heat flow,  $\chi_t$ . For simplicity, equal weight is given to each set of observations so that

$$\chi_t = \sqrt{\left( \frac{\chi_s^2 + \chi_h^2}{2} \right)}. \quad (9)$$

We wish to revisit a range of both analytical and numerical plate models by using a combination of subsidence modeling, heat flow modeling and joint modeling. The purpose of investigating these different forms of modeling is to probe differences between proposed models in the context of the self-consistency of subsidence and heat flow measurements. In each case, we are interested in locating a global minimum which identifies the optimal values of  $T$ ,  $z_p$  and sometimes  $z_r$ . We are also interested in exploring any obvious trade-offs between these three parameters. Recovered values of these plate parameters are benchmarked against independent geologic constraints. For example, ambient mantle potential temperature has been estimated from petrologic and geochemical studies at mid-oceanic ridges (e.g. 1250–1350°C: Katsura et al. (2004); 1280–1400°C: Herzberg et al. (2007); 1350±50°C: Lee et al. (2009); 1318<sup>+44</sup><sub>-32</sub> °C: Matthews et al. (2016)). Dalton et al. (2014) provide a petrologic range of 1300–1550°C, which they refine to a range of 1314–1464°C (i.e. 1388±45°C) by including constraints provided by seismic velocity values and zero-age depths. The midpoint and range that qualitatively honors the common overlaps between these different estimates is 1332±18°C.

From a geodynamic perspective, equilibrium lithospheric thickness is a useful and important concept. However, it is difficult to independently and accurately constrain its value because the relationship between long-term mechanical properties and, say, seismic velocity is unclear. Some studies have either implicitly or explicitly estimated  $z_p$  by calibrating shear wave tomographic models against a plate cooling model, which, from the perspective of this contribution, represents a circular argument (Priestley & McKenzie, 2006; Priestley et al., 2024). Steinberger and Becker (2018) determine lithospheric thickness from the results of five earthquake tomographic models by identifying the depth to an empirically estimated isothermal surface (i.e. 1126°C). They obtain a mean thickness of equilibrium oceanic lithosphere of 109 ± 22 km. Burgos et al. (2014) use the results of a global surface wave dispersion study to suggest that the lithosphere-asthenosphere boundary beneath old oceanic plates commences at a depth of ∼100 km.

Although the zero-age depth at mid-oceanic ridges can be determined directly from subsidence observations, its average value is difficult to pinpoint since depths of mid-oceanic ridges vary by ±1 km or more, principally as a consequence of mantle dynamic topography. It is generally agreed that the mean global value is  $z_r = 2.5 \pm 0.3$  km which is what we use here (Parsons & Sclater, 1977; Stein & Stein, 1992; Rowley, 2019). Occasionally, we treat  $z_r$  as a quasi-independent parameter that can be extracted by inter-

rogating the joint misfit between observed and calculated subsidence and heat flow. In these instances, recovered values of  $z_r$  do not differ significantly from 2.5 km.

## 387 5 Results

### 388 5.1 Original Analytical Model (HWR-1)

389 Figure 4 presents the results of an analytical plate model, which adopts the exact  
 390 parameterization assumed by Parsons and Sclater (1977). Using this legacy parameter-  
 391 ization has two purposes. First, we wish to examine the effects of increasing the num-  
 392 ber and distribution of subsidence measurements upon this parameterization. Secondly,  
 393 we wish to investigate the impact of separately and jointly modeling subsidence and heat  
 394 flow data (Figure 4a-b). In their scheme, the value of mean thermal conductivity,  $k =$   
 395  $3.138 \text{ W m}^{-1} \text{ K}^{-1}$ , is based upon the laboratory experiments of Schatz and Simmons  
 396 (1972), schematically shown in Figure 3a. The value of mean heat capacity,  $C_p = 1171.52$   
 397  $\text{J K}^{-1}$ , is based upon measurements of typical minerals over a temperature range that  
 398 is appropriate for oceanic lithosphere (Goranson, 1942). Note that Parsons and Sclater  
 399 (1977) varied thermal expansivity to minimize the misfit between observed and calcu-  
 400 lated subsidence measurements. Their recovered value for combined subsidence model-  
 401 ing of the North Pacific and North Atlantic oceans is  $\alpha = (3.2 \pm 1.1) \times 10^{-5} \text{ K}^{-1}$ .

402 Our modeling strategy is implemented in three steps. First, subsidence observa-  
 403 tions alone were fitted by systematically varying  $T$  and  $z_p$  where  $z_r$  is fixed at 2.5 km.  
 404 There is a weak global minimum at  $\chi_s < 0.2$  with a clear negative trade-off between  
 405  $T$  and  $z_p$  such that a thinner, hotter plate or a cooler, thicker plate fits the observations  
 406 equally well (Figure 4c). At the global minimum,  $T = 1375^\circ\text{C}$  and  $z_p = 106 \text{ km}$ . In com-  
 407 parison, Parsons and Sclater (1977) obtained  $T = 1350^\circ\text{C}$  and  $z_p = 125 \text{ km}$ . Minor dif-  
 408 ferences reflect the fact that Parsons and Sclater (1977) exploit 377 age-depth measure-  
 409 ments from the North Pacific and North Atlantic oceans whereas our global database  
 410 contains 10,863 measurements. Comparison of Figure 4a and f shows that the average  
 411 slope of their 377 measurements is slightly steeper. Although this difference is small, it  
 412 acts to displace our estimates of  $T$  and  $z_p$  to higher and thinner values, respectively. Sec-  
 413 ondly, heat flow observations are fitted. In this case, we obtain  $T = 1375^\circ\text{C}$  and  $z_p =$   
 414  $81 \text{ km}$  (i.e. a thinner plate; Figure 4d).

415 Finally, we jointly fit subsidence and heat flow observation which yields  $T = 1474^\circ\text{C}$   
 416 and  $z_p = 95 \text{ km}$  at the global minimum of  $\chi_t = 0.248$  (Figure 4e). This joint fitting yields  
 417 a temperature that is  $\sim 100^\circ\text{C}$  hotter and a thinner plate. Figure 4e demonstrates that  
 418 Stein and Stein (1992) obtained very similar values of  $T = 1450^\circ\text{C}$  and  $z_p = 95 \text{ km}$  with  
 419 a thermal expansion coefficient of  $\alpha = 3.1 \times 10^{-5} \text{ K}^{-1}$ . Although they exploited dif-  
 420 ferent global databases of subsidence and heat flow measurements, the principal reason  
 421 for this close similarity is the fact that, in both cases, joint fitting of subsidence and heat  
 422 flow observations has been carried out assuming  $k = 3.138 \text{ W m}^{-1} \text{ K}^{-1}$ , which results  
 423 in a thinner, hotter plate.

424 Figure 4f and g show the original subsidence and heat flow measurements of Parsons  
 425 and Sclater (1977). These observations include 377 age-depth measurements and 29 heat  
 426 flow measurements. Figure 4h demonstrates that the global minimum obtained by fit-  
 427 ting subsidence measurements occurs at  $T = 1350^\circ\text{C}$  and  $z_p = 125 \text{ km}$  (i.e. identical to  
 428 the values recovered by Parsons and Sclater (1977)). However, Figure 4i demon-  
 429 strates that the global minimum obtained by fitting heat flow observations occurs at  $T = 1457^\circ\text{C}$   
 430 and  $z_p = 96 \text{ km}$ . Note that, in this case, misfit was only calculated using heat flow mea-  
 431 surements  $>60 \text{ Ma}$  in order to negate the influence of hydrothermal circulation which  
 432 affects young oceanic crust. Similarly, joint modeling yields  $T = 1481^\circ\text{C}$  and  $z_p = 102 \text{ km}$   
 433 (Figure 4j). This result highlights the fact that combined modeling of subsidence and  
 434 heat flow measurements tends to generate an optimal model with an excessively high tem-

perature (see also Stein and Stein (1992)). This result is a direct consequence of formally fitting heat flow measurements, which Parsons and Sclater (1977) did not implement although they did use their subsidence-based model to predict heatflow variation.

In summary, there are two obvious problems that are highlighted by our three-step analysis (Figure 4). First, parameter values recovered by separately fitting subsidence and heat flow observations are strikingly different—subsidence observations tend to predict a thicker plate and heat flow observations predict a thinner plate. Secondly, joint fitting of subsidence and heat flow measurements does not yield parameter values that are consistent with independent constraints, particularly with respect to the recovered basal temperature which is  $\sim 150^{\circ}\text{C}$  hotter than expected. This exceptionally hot basal temperature is strongly influenced by the fitting of heat flow measurements, which yields a very thin plate ( $<100$  km) for all basal temperatures.

## 5.2 Revised Analytical Model (HWR-2)

The mismatch between parameter values recovered from both separate and joint modeling of subsidence and heat flow measurements indicates that the original parameterization of Parsons and Sclater (1977) requires some modification. This mismatch arises because, for a given geothermal profile, subsidence is sensitive to the average value of thermal conductivity that is obtained by integration over the total thickness of the cooling lithosphere whereas surface heat flow is also sensitive to the value of thermal conductivity toward the top of the lithosphere (compare Equations 3 and 4).

The value of  $k$  assumed by Parsons and Sclater (1977) is  $3.138 \text{ W m}^{-1} \text{ K}^{-1}$ . It is a mean value for the upper 120 km of the mantle (Schatz & Simmons, 1972). The simplest approach is to identify a suitable average value of  $k$ , which can reconcile the mismatch that has arisen by systematically varying  $k$  between  $3.20$  and  $4.10 \text{ W m}^{-1} \text{ K}^{-1}$  at intervals of  $0.1 \text{ W m}^{-1} \text{ K}^{-1}$ . For  $k = 3.8 \text{ W m}^{-1} \text{ K}^{-1}$ , a global minimum of  $\chi_t = 0.247$ , obtained by jointly fitting subsidence and heat flow observations, is located at  $T = 1326^{\circ}\text{C}$  and  $z_p = 105$  km when  $z_r$  is fixed at 2.5 km (Figures 5a-e and 3a). This average value of  $k$  falls within the bounds of experimental and geologic uncertainty (see, e.g., Grose and Afonso (2013); Richards et al. (2018); Figure 6a).

In contrast to the HWR-1 plate model, the recovered value of  $T=1326^{\circ}\text{C}$  is now in excellent agreement with that determined from independent petrologic and geochemical studies (i.e.  $T_p=1332\pm18^{\circ}\text{C}$ ; Figure 5e). A slightly higher value of mean thermal conductivity is justified by examining experimental measurements (Hofmeister, 1999, 2005; Pertermann & Hofmeister, 2006). For example, Pertermann and Hofmeister (2006) use a laser flash technique which yields higher thermal conductivity values throughout the lithosphere compared with the original measurements of Schatz and Simmons (1972). The mean thermal conductivity from laser flash experiments is  $k = 3.6 \text{ W m}^{-1} \text{ K}^{-1}$  (Figure 6a). This value assumes no radiative component which, if included, could significantly increase the mean thermal conductivity of the lithosphere. The recovered value of lithospheric thickness,  $z_p = 105\pm10$  km, equates to a thickness of  $\sim 90$  km for a basal temperature of  $1126^{\circ}\text{C}$  which is at the lower bound of, but still broadly consistent with, independent estimates of equilibrium lithospheric thickness ( $z_p = 109\pm22$  km; Steinberger and Becker (2018)). Priestley et al. (2024) constructed steady state geothermal profiles from temperature estimates, which were obtained by calibrating global shear-wave velocity measurements. At one location on old Pacific oceanic crust ( $\sim 140$  Ma), their calculated lithospheric thickness (equivalent to equilibrium plate thickness) is 104 km.

In order to sidestep any possible effects of efficient hydrothermal circulation close to the ridge axis, we match the approach of Richards et al. (2018) by excluding subsidence and heat flow observations from seafloor younger than 5 Ma. We also fix the value of  $z_r$  at 2.5 km. Critically, the effects of fixing  $z_r$  and of excluding measurements from the youngest lithosphere are easily tested. First, we allow  $z_r$  to vary, which yields  $T =$

486 1349°C,  $z_p = 105$  km and  $z_r = 2.45$  km (Figure 5f-h). Secondly, we can then include sub-  
 487 sidence values younger than 5 Ma, which yields  $T = 1347^\circ\text{C}$ ,  $z_p = 106$  km and  $z_r = 2.45$  km  
 488 (Figure 5i-k). In both cases, the recovered values of  $T$  still agree with those estimated  
 489 from independent petrologic and geochemical studies (i.e.  $T_p=1332\pm18^\circ\text{C}$ ). The recov-  
 490 ered values for  $z_p$  are almost identical. We conclude that permitting the value of  $z_r$  to  
 491 vary yields a slightly higher  $T$  whilst excluding measurements from seafloor that is younger  
 492 than 5 Ma has no discernible influence upon the recovered plate model.

### 493 5.3 Temperature- and Pressure-dependent Model (HWR-3)

494 Notwithstanding the fact that the simple HWR-2 analytical model yields an ex-  
 495 cellent fit between observed and calculated values of subsidence and heat flow, we ac-  
 496 knowledge that there is some interest in developing more sophisticated (i.e. physically  
 497 realistic) plate models. One reason concerns the detailed temperature structure of the  
 498 evolving plate, which can change significantly depending upon the specific thermal parametriza-  
 499 tion employed. For example, the recovered temperature structure can influence the em-  
 500 pirical relationship between temperature and shear wave velocity (Priestley & McKen-  
 501 zie, 2006).

502 The starting point concerns the results of laboratory experiments, which clearly  
 503 demonstrate that  $\alpha$ ,  $k$  and  $C_p$  vary as a function of temperature and pressure (Figure  
 504 6; McKenzie et al. (2005); Richards et al. (2018)). Here, we use a modified version of the  
 505 temperature- and pressure-dependent parameterization implemented by Richards et al.  
 506 (2018), which itself is a revised version of earlier parameterizations developed by McKenzie  
 507 et al. (2005) and by Grose and Afonso (2013). A useful summary of laboratory exper-  
 508 iments is provided by Figure 7 of Richards et al. (2020). Our changes are as follows—  
 509 the temperature-dependence of  $k$  is based on the lattice conductivity with a negligible  
 510 radiative component (Figure 3c; Figure 6a); the temperature-dependence of  $\alpha$  is taken  
 511 from Figure 3 of Bouhifd et al. (1996) rather than from their Table 2 (values quoted in  
 512 table and shown in figure are mutually inconsistent; Figure 6b); and the parameteriza-  
 513 tion of  $C_p$  is chosen so that olivine consists of 89% forsterite and 11% fayalite (Berman  
 514 and Aranovich (1997); Figure 6c). Figure 6 is a schematic summary of the chosen pa-  
 515 rameterization, the details of which are described in considerable detail by Richards et  
 516 al. (2020). Oceanic crust is assumed to act as an insulating layer in accordance with Grose  
 517 and Afonso (2013). However, we reduce the average crust thickness to 6.4 km in accor-  
 518 dance with Christeson et al. (2019) and with Holdt et al. (2022).

519 A revised plate model is presented in Figure 7. An optimal model obtained by jointly  
 520 fitting subsidence and heat flow observations is located at  $T = 1326^\circ\text{C}$ ,  $z_p = 96$  km and  
 521  $z_r = 2.80$  km where  $\chi_t = 0.195$ . In this instance, the value of  $z_r$  is also obtained by op-  
 522 timization. From the perspective of statistical tolerance, this result is in close agreement  
 523 with that obtained using the HWR-2 analytical model. Note that the decrease in the value  
 524 of  $\chi_t$  is statistically insignificant, that the decrease in equilibrium plate thickness from  
 525 105 km to 96 km is minor, and that there is no change in the value of  $T$ . The recovered  
 526 value of  $z_r$  falls within the range of observed mean ridge depth values (i.e.  $2.5 \pm 0.3$  km).

## 527 6 Discussion

528 Databases of age-depth and heat flow measurements can be satisfactorily fitted us-  
 529 ing any one of the three models presented here. Both the HWR-2 and HWR-3 models  
 530 recover basal and potential temperatures that honor independent petrologic constraints.  
 531 The significant reduction in the recovered basal temperature value between the HWR-  
 532 1 model ( $T = 1474^\circ\text{C}$ ) and the HWR-2 model ( $T = 1326^\circ\text{C}$ ) highlights the sensitivity  
 533 of any plate model to the parameterization of conductivity. Compared with HWR-3, HWR-  
 534 2 is clearly a very simple model in terms of parameterization. Although  $k$ ,  $\alpha$  and  $C_p$  vary  
 535 as a function of temperature and, to a lesser extent, pressure, both plate subsidence and

heat flow principally depend upon integrated averages of these parameters. In other words, unlike seismic constraints on thermal structure, these surface observations are largely (but not entirely) insensitive to the detailed functional variation of each parameter. The HWR-3 model adopts a more sophisticated parameterization, which incorporates the temperature- and pressure-dependence of  $k$ ,  $\alpha$  and  $C_p$ . Laboratory results obtained using either the contact method or laser flash analysis show that  $k$  increases significantly at low temperatures (i.e.  $5.5\text{--}7.0 \text{ W m}^{-1} \text{ K}^{-1}$ ; (Schatz & Simmons, 1972; Pertermann & Hofmeister, 2006)). This increase perturbs the recovered value of basal temperature, pushing it outside the independently accepted range (Figure 7h). One solution is incorporation of an insulating crust whose thermal properties remain, in turn, uncertain (see Figure 7a of Richards et al. (2018) for further details). The addition of an insulating crustal layer increases the recovered basal temperature from  $T = 1174^\circ\text{C}$  to  $T = 1326^\circ\text{C}$  (Figure 7e,h). This change demonstrates the sensitivity of plate models to the adopted conductivity structure, especially when fitting heat flow constraints. The result highlights the importance of accurate laboratory experiments for  $k$ ,  $\alpha$  and  $C_p$  on realistic aggregates of crustal and mantle rocks.

Reference models for cooling and subsidence of oceanic lithosphere have necessarily evolved as observational constraints improve and methodologies become more sophisticated. In Table 2, the databases exploited by key reference models together with values of assumed and recovered parameters are listed. Since the seminal analysis of Parsons and Sclater (1977), it is evident that increasing amounts of subsidence and heat flow measurements have been used to calculate optimal plate cooling models. Figure 8a summarizes the basal temperature estimates and the equilibrium lithospheric thicknesses predicted by the reference models listed in Table 2. Both the HWR-1 and the Stein and Stein (1992) models yield basal temperatures that significantly exceed independent petrologic estimates (Figure 8b). We contend that this discrepancy is a direct consequence of joint inverse modeling where the value of  $k$  may be too low. Richards et al. (2018) obtained an equilibrium plate thickness of 136 km with a basal temperature of  $1302^\circ\text{C}$ . We now believe that this plate thickness is likely to be excessively thick, which is the direct consequence of two factors. First, the isostatic sedimentary correction employed by Hoggard et al. (2017) gives rise to a modest overprediction of subsidence for old plate ages. A revised sedimentary correction, which assumes a smaller (i.e., siltier) value of solid grain velocity, has been proposed and implemented by Holdt et al. (2022). This rather minor adjustment slightly decreases the gradient of water-loaded subsidence for plate ages  $> 100 \text{ Ma}$ , which in turn yields a thinner equilibrium plate thickness. The adjustment highlights the importance of accurate age-depth measurements. Secondly, Richards et al. (2018) include ‘site-specific’ heat flow measurements for plate ages of 0–25 Ma. However, many of these measurements are from the Gulf of Aden, where some heat flow measurements may be anomalously elevated due to their proximity to the Afar mantle plume. By fitting these anomalous heat flow values, the optimal plate model must include a steep gradient to match older heat flow measurements, which necessarily yields a much thicker plate. Here, we do not exclusively use ‘site-specific’ measurements between 0–25 Ma. Instead, we exploit the global suite of measurements from Hasterok (2013), with their concomitantly greater uncertainty ranges, during this interval (compare Figure 7b with Figure 8b from Richards et al. (2018)). Figure 8 shows that several plate models yield acceptable values of basal temperature. Of these, we equally favor the HWR-2 and HWR-3 models which yield optimal fits to the latest available global databases of age-depth measurements and of revised heat observations. HWR-2 has the advantage of simplicity, while HWR-3 captures known temperature and pressure dependencies of key physical properties, which probably yields a more reliable thermal structure as a function of time.

We emphasize the importance of exploiting a global database of age-depth measurements to obtain a global average plate model. Clearly, this global database masks significant regional anomalies that are generally interpreted as mantle dynamic topographic

signals. Holdt et al. (2022) mapped the amplitudes and wavelengths of these positive and negative anomalies, which are associated with large-scale and small-scale mantle convective upwellings and downwellings (e.g. Icelandic Plume, Australian-Antarctica Discordance). Notwithstanding these important regional anomalies, it has also been proposed that transient (but global) age-depth shallowing exists. Age-depth measurements from the North Pacific Ocean were used by both Parsons and Sclater (1977) and by Stein and Stein (1992) to constrain their plate cooling models. Building upon these analyses, Crosby et al. (2006) exploited more detailed age-depth measurements from this region to propose that transient shallowing of  $\sim 250$  m occurs for plate ages of 80–130 Ma. This reference model is generated by using an empirical fit to water-loaded age-depth observations. Critically, anomalous observations were removed by excising regions in which substantial long wavelength free-air gravity anomalies correlate with bathymetry. Crosby et al. (2006) also report similar shallowing in four other regions of the oceanic realm. Figure ??c shows that the transient shallowing observed by Crosby et al. (2006) is evident within our database—it is clearly visible when the global subsidence database of Holdt et al. (2022) is sampled within the North Pacific Ocean (Figure 10a). The amplitude and wavelength of the recovered shallowing are almost identical (compare Figure ??c and d). Note that the database of Stein and Stein (1992), which includes age-depth measurements from the North Pacific Ocean, also shows transient shallowing between  $\sim 100$  and 130 Ma (see their Figure 1b). Figure 10 shows that the North Pacific Ocean features positive residual depth anomalies in the vicinity of various hotspot tracks within this 80–130 Ma window. In addition, the observed shallowing of age-depth measurements in this region becomes emergent because only one flank of the cooling plate has been sampled (Figure 10b). Several other regions were also used by Crosby et al. (2006) to demonstrate transient shallowing. However, these smaller regions tend to feature the same age-depth sampling pathology. Figure 10c shows that these regions also feature mantle plumes within the 80 and 130 Ma age window: the Bermuda swell of the Northwest Atlantic Ocean; the Cape Verde, Madeira and New England swells of the Northeast Atlantic Ocean; and the Angolan and Vema swells of the Southwest Atlantic Ocean. Figure 10 c also shows that these regions do not include significant downwellings which lie within the 80–130 Ma window (e.g., Argentine Abyssal Plain, Weddell Sea, Bay of Bengal). Figure 2b demonstrates that transient shallowing is not evident on a global scale, presumably because positive and negative regional anomalies are averaged out on a global scale.

The overall flattening of global age-depth measurements to a water-loaded depth of 6 km from approximately 80 Ma is matched by a flattening of heat flow measurements, which tend towards  $0.05 \text{ W m}^{-2}$  at old plate ages. Parsons and McKenzie (1978) suggest that the oceanic lithosphere consists of mechanical and thermal boundary layers. As the plate cools, both of these layers thicken with age. From a fluid dynamical perspective, the thermal boundary layer should become unstable and convectively overturn for plate ages that exceed about 60 Ma. A convective instability is invoked by Parsons and McKenzie (1978) in order to stabilize lithospheric thickness. We suggest that instabilities occur on smaller length scales and therefore on shorter timescales than hitherto expected, such that they cryptically lie within the scatter produced by residual depth anomalies.

We end this contribution by addressing the rheological structure of cooling oceanic lithosphere. Figure 11a and b show the evolving thermal structure of oceanic lithosphere calculated for the HWR-2 and HWR-3 models, respectively. In both cases, the distribution of intraplate and outer rise earthquakes analyzed by Craig et al. (2014) occur at temperatures of  $< 700^\circ\text{C}$ , in broad agreement with some, but not all, previous studies (McKenzie et al., 2005; Craig et al., 2014; Richards et al., 2018). This revised estimate is now consistent with laboratory creep experiments carried out upon dry polycrystalline olivine aggregates (Goetze & Evans, 1979; Boettcher et al., 2007). At greater depths, our recovered temperature structure can be compared with the surface wave dispersion results of Burgos et al. (2014). They suggest that the lithosphere-asthenosphere bound-

644       ary layer can be identified using a combination of two proxies—vertically polarized shear  
645       wave velocity measurements,  $V_{sv}$ , and orientations of the fast axis of azimuthal anisotropy,  
646        $\psi_G$ . For oceanic lithosphere older than  $\sim 60$  Ma, the top of the lithosphere–asthenosphere  
647       boundary layer identified by measurements of  $\psi_G$  broadly coincides with a predicted tem-  
648       perature of about  $1300^{\circ}\text{C}$  or falls just beneath the base of the plate (Figure 11a and b).  
649       Note that  $\psi_G$  measurements exhibit a flattening with age from 80 Ma of both the up-  
650       per and lower bounds of the measured cloud. This observation is broadly consistent with  
651       age-depth and heat flow measurements.

## 652       7 Conclusions

653       In this study, a global database of accurate age-depth measurements is combined  
654       with an existing database of filtered heat flow measurements to revisit the well-known  
655       plate cooling model. Our primary goal is to identify the simplest plate model that yields  
656       the smallest misfit between combined age-depth and heat flow measurements. In order  
657       to accomplish this task, we have explored a variety of analytical and numerical plate mod-  
658       els which respectively assume that thermal conductivity, thermal expansivity and spe-  
659       cific heat capacity are constant or vary as a function of temperature and pressure using  
660       experimental constraints. The optimal analytical model yields a basal temperature of  
661        $1326 \pm 50^{\circ}\text{C}$  and an equilibrium plate thickness of  $105 \pm 10$  km for a zero-age depth  
662       of  $2.50 \pm 0.3$  km. This value of basal temperature is consistent with independent con-  
663       straints. A more physically accurate numerical model fits subsidence and heat flow ob-  
664       servations equally well and yields almost identical values of basal temperature and equi-  
665       librium plate thickness. Spatial analysis of our global database of age-depth measure-  
666       ments shows that previously described transient shallowing for plate ages of 80–130 Ma  
667       is a product of geographic sampling. This lack of shallowing suggests that convective in-  
668       stabilities, which are thought to maintain constant plate thickness, probably act on shorter  
669       timescales and smaller length scales. Finally, our revised plate model can be used to cal-  
670       culate the thermal structure of the lithosphere as a function of time, to estimate that  
671       the maximum depth of intraplate earthquakes is bound by the  $700^{\circ}\text{C}$  isothermal surface,  
672       and to accurately estimate residual depth anomalies which represent maximum observ-  
673       able mantle dynamic topography.

**Table 1.** Symbols and Values of Parameters.

	Symbol	Parameter	Value	Units
Thermal parameters	$\alpha$	Thermal expansivity	-	$K^{-1}$
	$C_p$	Heat capacity	-	$J K^{-1}$
	$k$	Thermal conductivity	-	$W m^{-1} K^{-1}$
Recovered parameters	$T$	Mantle temperature	-	$^{\circ}C$
	$T_b$	Mantle basal temperature	-	$^{\circ}C$
	$T_p$	Mantle potential temperature	-	$^{\circ}C$
	$z_p$	Equilibrium lithospheric thickness	-	km
	$z_r$	Water-loaded ridge depth	-	km
Observed subsidence	$w$	Water-loaded basement depth	-	km
	$C_c$	Crustal correction	-	km
	$C_s$	Sediment correction	-	km
	$z_{sb}$	Depth of seabed	-	km
Observed heat flow	$H$	Heat flow	-	$W m^{-2}$
	$\Delta T/\Delta z$	Thermal gradient	-	$^{\circ}C / m$
	$F$	Perturbation of geotherm	-	dimensionless
	$\kappa_s$	Thermal diffusivity of sediment	0.25	$mm^2 s^{-1}$
	$t_s$	Duration of sedimentation	-	Ma
General	$U$	Sedimentation rate	-	$km Ma^{-1}$
	$t$	Time	-	Ma
	$z$	Depth	-	km
	$T$	Temperature	-	$^{\circ}C$
	$P$	Pressure	-	MPa
Calculated subsidence; calculated heat flow	$X$	Composition	-	
	$\rho$	Density	-	$Mg m^{-2}$
	$\rho_m$	Density of mantle at $0^{\circ}C$	3.30	$Mg m^{-2}$
	$\rho_w$	Density of water	1.03	$Mg m^{-2}$
	$T_0$	Surface temperature	0	$^{\circ}C$
	$\kappa$	Thermal diffusivity	-	$mm^2 s^{-1}$
	$\rho_b$	Density at depth of compensation	-	$Mg m^{-2}$
	$\Delta t$	Time interval between nodes	-	Ma
	$\Delta z_0^n$	Depth interval between nodes	-	km
	$k_0^n$	Surface conductivity	-	$W m^{-1} K^{-1}$
Misfit calculation	$T_0^n$	Surface temperature	-	$^{\circ}C$
	$T_1^n$	Temperature at next deepest node	-	$^{\circ}C$
	$\chi_s$	Subsidence misfit	-	dimensionless
	$\chi_h$	Heat flow misfit	-	dimensionless
	$\chi_t$	Joint misfit	-	dimensionless
	$w_i^o$	Observed subsidence	-	km
	$w_i^c$	Calculated subsidence	-	km
	$N_s$	Number of subsidence age bins	65	dimensionless
	$\sigma_i$	Interquartile range of subsidence age bin	-	km
	$H_i^o$	Observed heat flow	-	$W m^{-2}$
	$H_i^c$	Calculated heat flow	-	$W m^{-2}$
	$N_h$	Number of heat flow age bins	65	dimensionless
	$\sigma_i^*$	Interquartile range of heat flow age bin	-	$W m^{-2}$

**Table 2. Reference models for evolution of oceanic lithosphere.**  $w$  = measurements of water-loaded basement depth;  $H$  = measurements of heat flow;  $k$  = thermal conductivity ( $\text{W m}^{-1}\text{K}^{-1}$ );  $\alpha$  = thermal expansivity ( $\times 10^{-5}\text{K}^{-1}$ );  $C_p$  = heat capacity ( $\text{J K}^{-1}$ );  $T$  = Mantle temperature ( $^{\circ}\text{C}$ );  $z_p$  = equilibrium lithospheric thickness (km);  $z_r$  = ridge depth (km) Pac. = Pacific Ocean. Atl. = Atlantic Ocean. V = variable parameters. Bold values denote recovered parameters.

Name	Reference	Location	$w$	$H$	$k$	$\alpha$	$C_p$	$T$	$z_p$	$z_r$
PSM	Parsons and Sclater (1977)	N.Pac., N.Atl.	377	29	3.138	<b>3.20</b>	1171.52	<b>1350</b>	<b>125</b>	2.50
GDH1	Stein and Stein (1992)	N.Pac., NW.Atl.	Grid	5,539	3.138	<b>3.10</b>	1171.52	<b>1450</b>	<b>95</b>	2.60
CHABLIS	Doin and Fleitout (1996)	Global	Grid	853	3.100	<b>4.20</b>	1124.00	<b>1310</b>	<b>105</b>	2.50
HW05	Hillier and Watts (2005)	N.Pacific	Grid	<b>3.371</b>	<b>2.77</b>	1171.52	<b>1363</b>	<b>120</b>	<b>3.01</b>	
MJP05	McKenzie et al. (2005)	N/A	N/A	V	V	V	1315	<b>106</b>	2.50	
CMS06	Crosby et al. (2006)	N.Pacific	Grid	N/A	V	V	1315	90	2.65	
CM09	Crosby and McKenzie (2009)	Global	Grid	N/A	V	V	N/A	90	2.60	
RHWC18	Richards et al. (2018)	Global	2,028	3,597	V	V	V	<b>1302</b>	<b>136</b>	<b>2.64</b>
HWR-1	This study	Global	10,863	3,573	3.138	3.20	1171.52	<b>1474</b>	<b>95</b>	2.50
HWR-2	This study	Global	10,863	3,573	3.800	3.20	1171.52	<b>1326</b>	<b>105</b>	2.50
HWR-3	This study	Global	10,863	3,573	V	V	V	<b>1326</b>	<b>96</b>	<b>2.80</b>

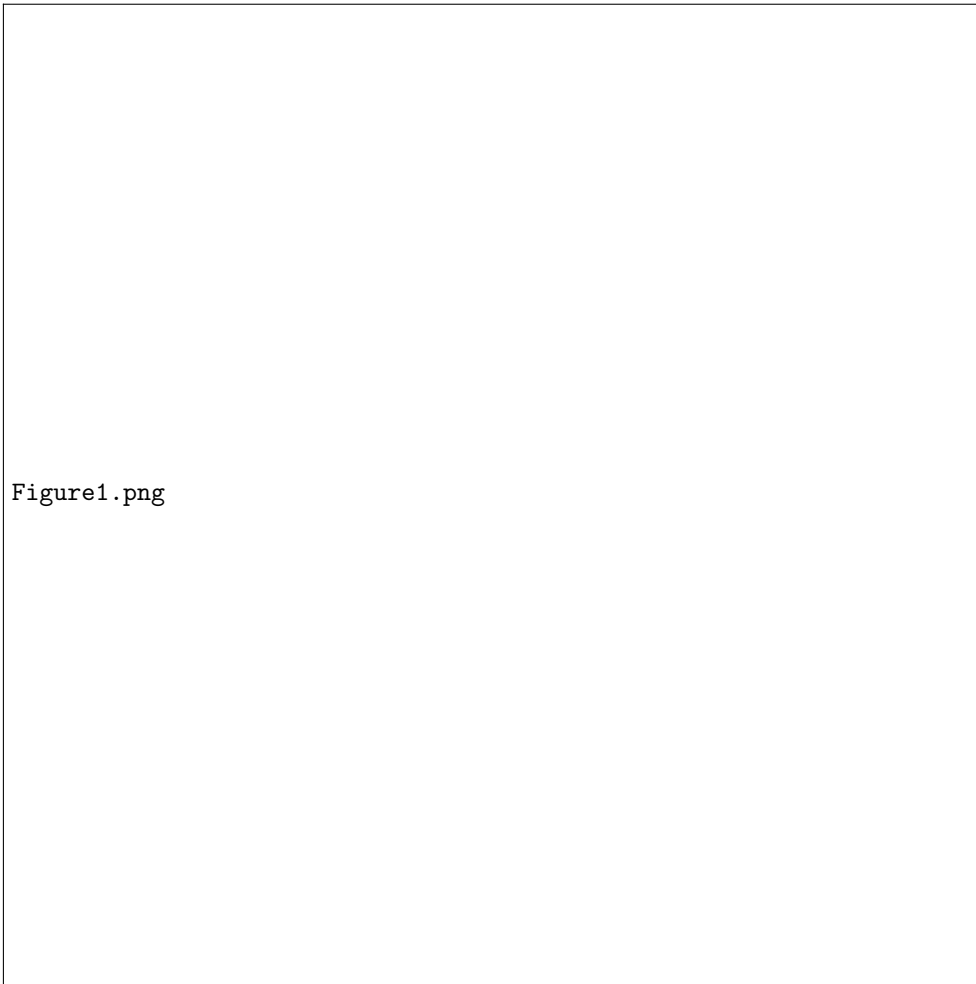
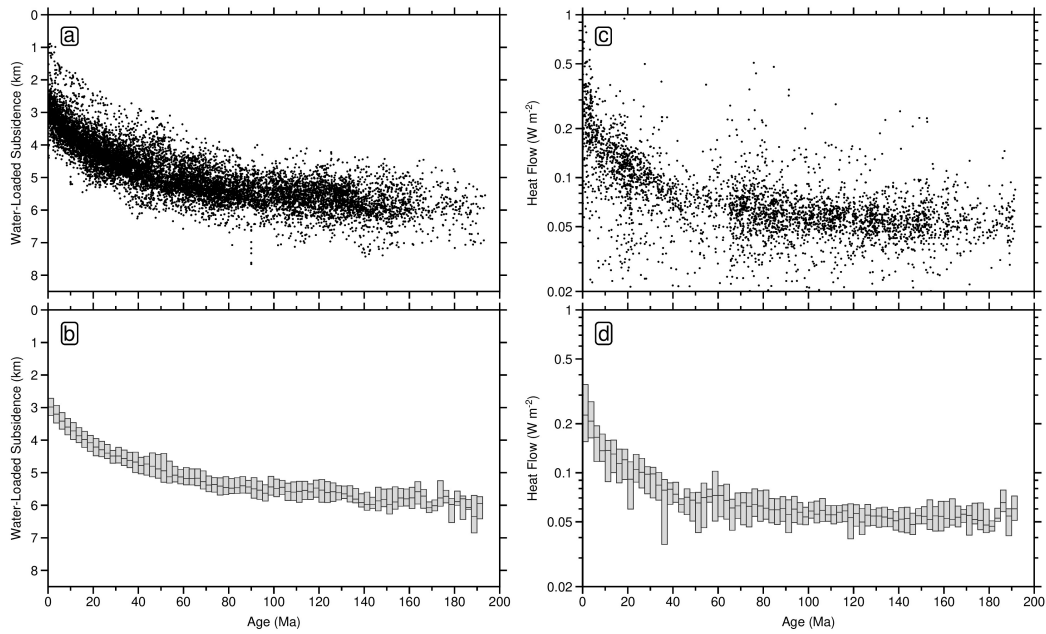
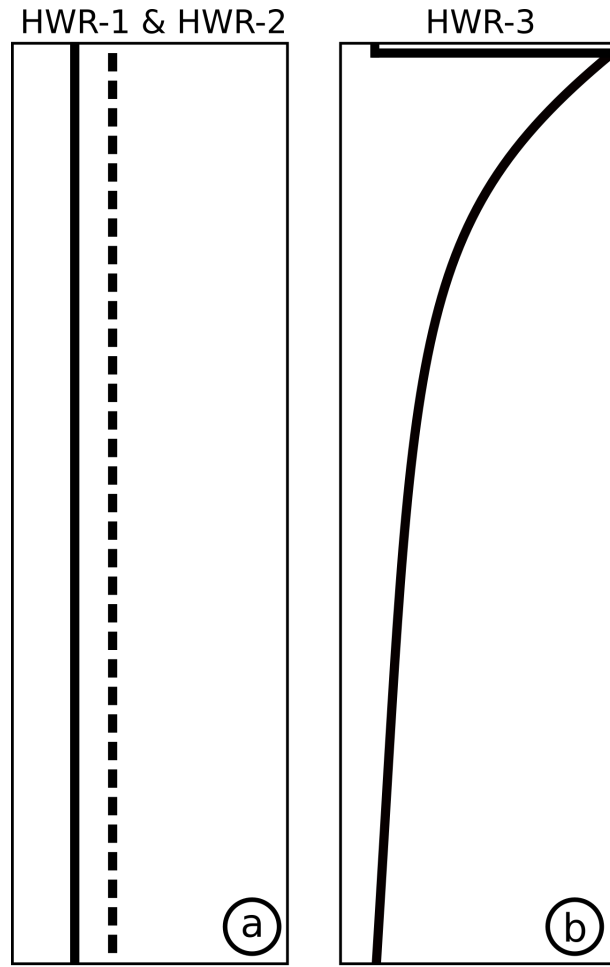


Figure1.png

**Figure 1. Global databases.** (a) Distribution of water-loaded depth to oceanic basement measurements, averaged within  $1^{\circ}$  bins (Holdt et al., 2022). Circles = accurate measurements obtained by applying both sedimentary and crustal corrections; upward/downward pointing triangles = lower/upper estimates obtained by applying sedimentary correction and regional crustal correction. (b) Distribution of heat flow measurements (Hasterok et al., 2011). Colored/gray circles = measurements that pass/fail filtering process. (c) Augmented age grid of Seton et al. (2020) that includes modifications based upon regional studies compiled by Hoggard et al. (2017) and Holdt et al. (2022).



**Figure 2. Age-depth and heat flow measurements as function of oceanic plate age.**  
 (a) Water-loaded measurements of depth to oceanic basement plotted as function of plate age and averaged within  $1^\circ$  bins (Holdt et al., 2022). See Figure 1a for global distribution. (b) Same measurements binned every 2.5 Ma. Horizontal bars with vertical gray boxes = median values with interquartile ranges. (c) Filtered and corrected heat flow measurements as function of plate age (Hasterok et al., 2011). See Figure 1b for global distribution. (d) Same measurements binned every 2.5 Ma. Horizontal bars with vertical gray boxes = median values with interquartile ranges.



**Figure 3. Cartoons showing different thermal conductivity parameterizations.**

(a) Models HWR-1 and HWR-2 where thermal conductivity is constant with depth; solid line = HWR-1; dashed line = HWR-2. Thermal conductivity is scaled between 2 and  $7 \text{ W m}^{-1} \text{ K}^{-1}$ . (b) Model HWR-3 where thermal conductivity varies as function of depth according to Pertermann and Hofmeister (2006) with insulating crustal layer (Grose & Afonso, 2013).

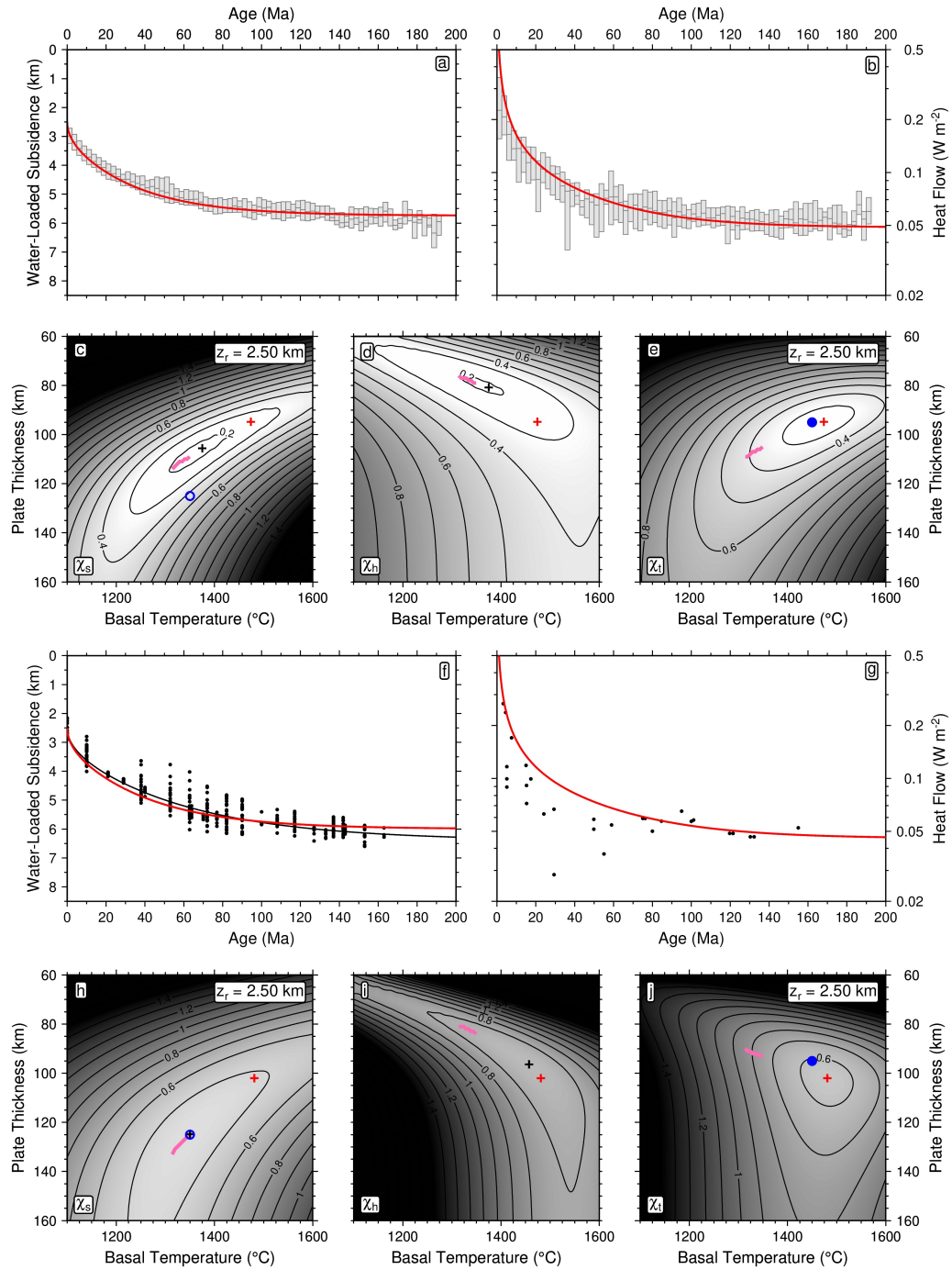


Figure 4. Caption overleaf.

---

**Figure 4. Analytical plate model using Parsons and Sclater (1977) parameterization (HWR-1).**

(a) Horizontal bars with vertical gray boxes = median values with interquartile ranges of age-depth measurements; red line = optimal fit between observed and calculated age-depth obtained by jointly fitting age-depth and heat flow measurements where  $T = 1474^\circ\text{C}$  and  $z_p = 95$  km, when  $z_r$  is fixed at 2.50 km. (b) Horizontal bars with vertical gray boxes = median values with interquartile ranges of heat flow measurements; red line = optimal fit between observed and calculated heat flow obtained by jointly fitting age-depth and heat flow measurements. (c) Misfit between observed and calculated age-depth,  $\chi_s$ , plotted as function of basal temperature and plate thickness when  $z_r$  is fixed at 2.50 km. Black cross = locus of global minimum; red cross = locus of global minimum shown in panel (e); open blue circle = locus of global minimum obtained by Parsons and Sclater (1977); pink line = loci of minima when basal temperature is fixed at  $1332 \pm 18^\circ\text{C}$ . (d) Misfit between observed and calculated heat flow,  $\chi_h$ . (e) Joint misfit between observed and calculated age-depth and heat flow,  $\chi_t$  when  $z_r$  is fixed at 2.50 km. Red cross = global minimum at  $T = 1474^\circ\text{C}$ ;  $z_p = 95$  km; Blue circle = locus of global minimum obtained by Stein and Stein (1992). (f) Black circles = original age-depth measurements of Parsons and Sclater (1977) from North Pacific and North Atlantic Oceans; red line = optimal fit between observed and calculated age-depth obtained by jointly fitting age-depth and heat flow measurements of Parsons and Sclater (1977) where  $T = 1481^\circ\text{C}$  and  $z_p = 102$  km, when  $z_r$  is fixed at 2.50 km; black line = optimal fit between observed and calculated age-depth obtained by Parsons and Sclater (1977) where  $T = 1350^\circ\text{C}$ ;  $z_p = 125$  km;  $z_r = 2.50$  km. (g) Black circles = original heat flow measurements of Parsons and Sclater (1977); red line = optimal fit between observed and calculated heat flow obtained by jointly fitting age-depth and heat flow measurements of Parsons and Sclater (1977). (h)–(j) Same as panels (c)–(e) where misfit is calculated using age-depth and heat flow measurements shown in panels (f) and (g).

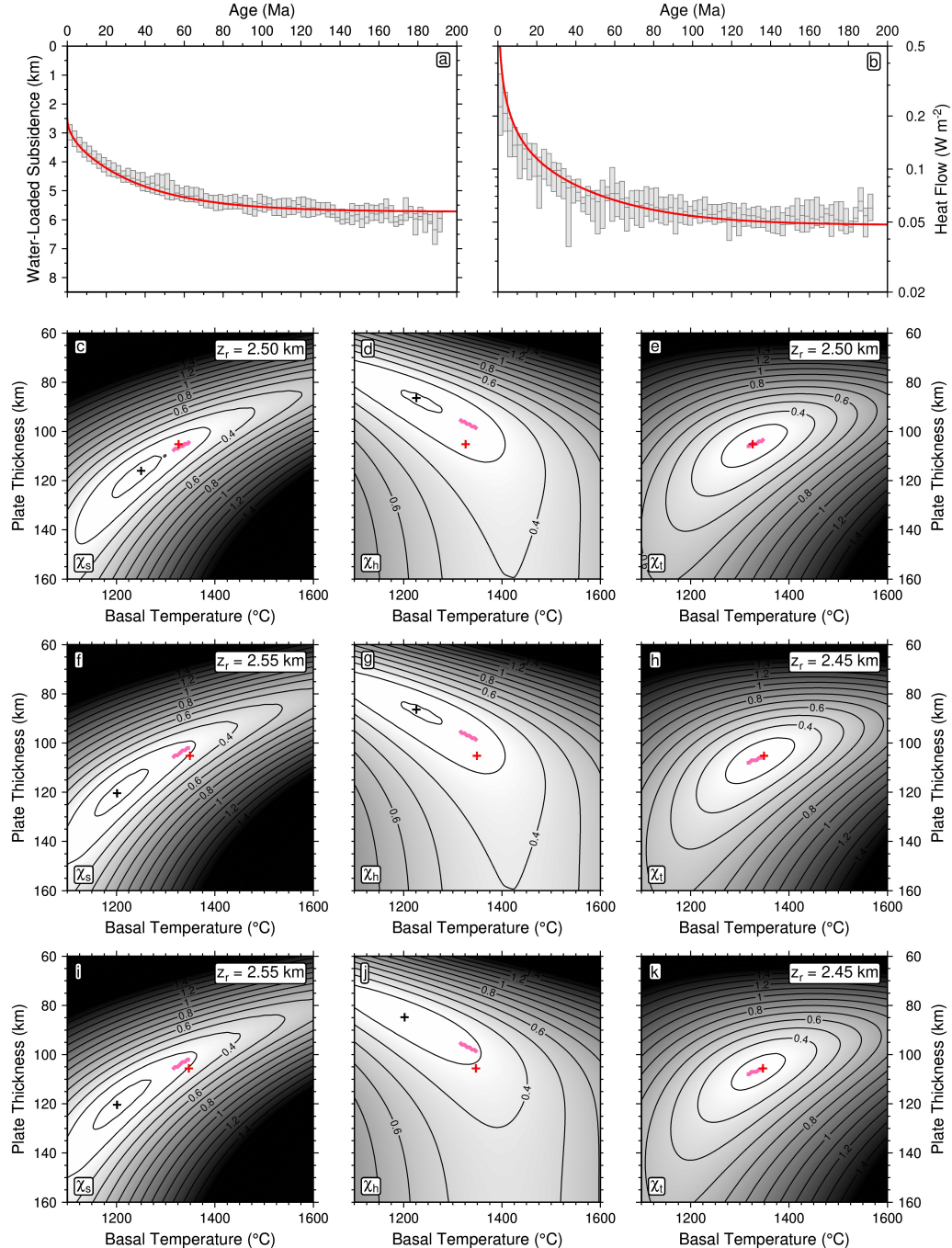
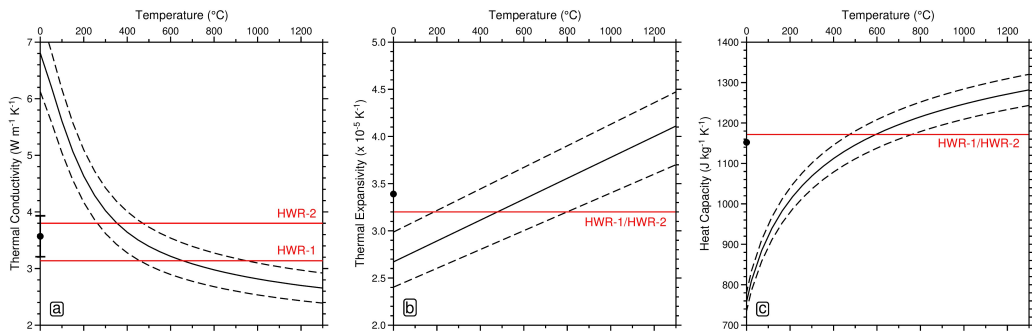


Figure 5. Caption overleaf.

---

**Figure 5. Revised analytical plate model with increased thermal conductivity (HWR-2).** (a) Horizontal bars with vertical gray boxes = median values with interquartile ranges of age-depth measurements; red line = optimal fit between observed and calculated age-depth obtained by jointly fitting age-depth and heat flow measurements where  $T = 1326^\circ\text{C}$  and  $z_p = 105$  km, when  $z_r$  is fixed at 2.50 km. (b) Horizontal bars with vertical gray boxes = median values with interquartile ranges of heat flow measurements; red line = optimal fit between observed and calculated heat flow obtained by jointly fitting age-depth and heat flow measurements. (c) Misfit between observed and calculated age-depth,  $\chi_s$ , plotted as function of basal temperature and plate thickness when  $z_r$  is fixed at 2.50 km. Black cross = locus of global minimum; red cross = locus of global minimum shown in panel (e); pink line = loci of minima when basal temperature is fixed at  $1332 \pm 18^\circ\text{C}$ . Note that age-depth measurements between 0 and 5 Ma are excluded, and the ridge depth is fixed at 2.50 km. (d) Misfit between observed and calculated heat flow,  $\chi_h$ . Note that heat flow measurements between 0 and 5 Ma are excluded. (e) Joint misfit between observed and calculated age-depth and heat flow,  $\chi_t$ , when  $z_r$  is fixed at 2.50 km. (f)–(h) Same as panels (c)–(e) except that  $z_r$  is variable. Note that locus of global minimum obtained by jointly fitting age-depth and heat flow measurements shifts very slightly to  $T = 1349^\circ\text{C}$ ;  $z_p = 105$  km;  $z_r = 2.45$  km. (i)–(k) Same as panels (c)–(e) except that  $z_r$  is variable, and both age-depth and heat flow measurements between 0 and 5 Ma are now included. Note that locus of global minimum obtained by jointly fitting age-depth and heat flow measurements shifts very slightly to  $T = 1347^\circ\text{C}$ ;  $z_p = 106$  km;  $z_r = 2.45$  km.



**Figure 6. Plate model parameterization.** (a) Thermal conductivity plotted as function of temperature. Solid/dashed black lines = forsterite lattice conductivity measurements  $\pm 10\%$  uncertainty at constant pressure of 0.1 MPa, redrawn from Pertermann and Hofmeister (2006); red lines = constant thermal conductivities assumed for HWR-1 and HWR-2; black circle with uncertainty = mean thermal conductivity value calculated between 0 and 1300°C, based upon parameterization of Pertermann and Hofmeister (2006) with  $\pm 10\%$  uncertainty. (b) Thermal expansivity plotted as function of temperature. Solid/dashed black lines = thermal expansivity measurements  $\pm 1\sigma$  for constant pressure of 0.1 MPa, taken from Figure 3 of Bouhifd et al. (1996); red line = constant thermal expansivity assumed for HWR-1 and HWR-2 models; black circle = mean thermal expansivity value calculated between 0 and 1300°C, based upon parameterization of Bouhifd et al. (1996). (c) Heat capacity plotted as function of temperature. Solid/dashed black lines = heat capacity measurements  $\pm 3\%$  uncertainty using parameterization of Berman and Aranovich (1997), which assumes 89% forsterite and 11% fayalite; red line = constant heat capacity assumed for HWR-1 and HWR-2 models; black circle = mean heat capacity value calculated between 0 and 1300°C, based upon parameterization of Berman and Aranovich (1997).

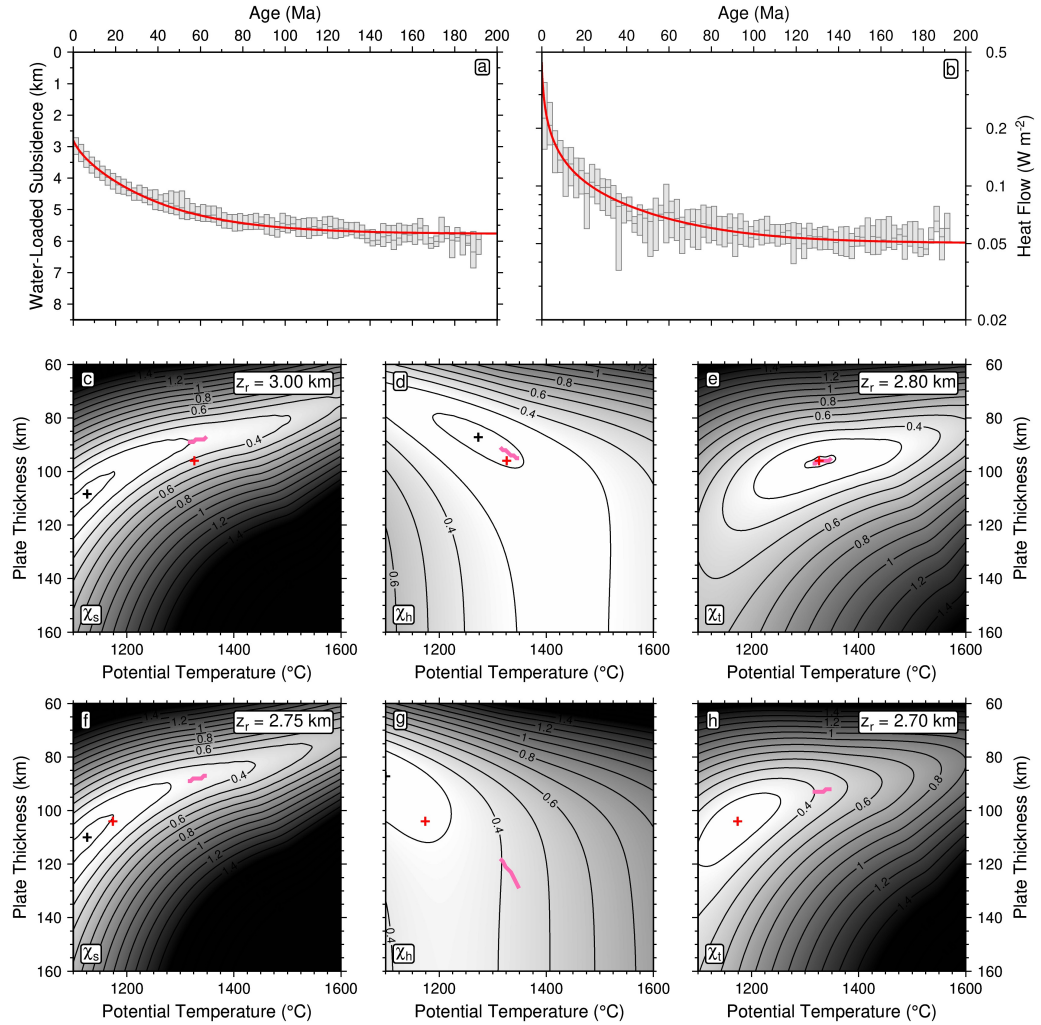


**Figure 7. Plate model with temperature- and pressure-dependent parameters (HWR-3).** (a) Horizontal bars with vertical gray boxes = median values with interquartile ranges of age-depth measurements; red line = optimal fit between observed and calculated age-depth obtained by jointly fitting age-depth and heat flow measurements where  $T = 1326^\circ\text{C}$ ;  $z_p = 96$  km;  $z_r = 2.80$  km. (b) Horizontal bars with vertical gray boxes = median values with interquartile ranges of heat flow measurements; red line = optimal fit between observed and calculated heat flow obtained by jointly fitting age-depth and heat flow measurements. (c) Misfit between observed and calculated age-depth,  $\chi_s$ , plotted as function of basal temperature and plate thickness for  $z_r = 3.00$  km. Black cross = locus of global minimum; red cross = locus of global minimum shown in panel (e); pink line = loci of minima when basal temperature is fixed at  $1332 \pm 18^\circ\text{C}$ . (d) Misfit between observed and calculated heat flow,  $\chi_h$ . (e) Joint misfit between observed and calculated age-depth and heat flow,  $\chi_t$ , for  $z_r = 2.80$  km. (f)–(h) Same as panels (c)–(e) except that insulating oceanic crustal layer is not included. In this case, optimal fit obtained by jointly fitting age-depth and heat flow measurements yields  $T = 1174^\circ\text{C}$ ;  $z_p = 104$  km;  $z_r = 2.70$  km. Note that basal temperature is expressed here as potential temperature since adiabatic gradient is included for HWR-3 (Richards et al., 2018).

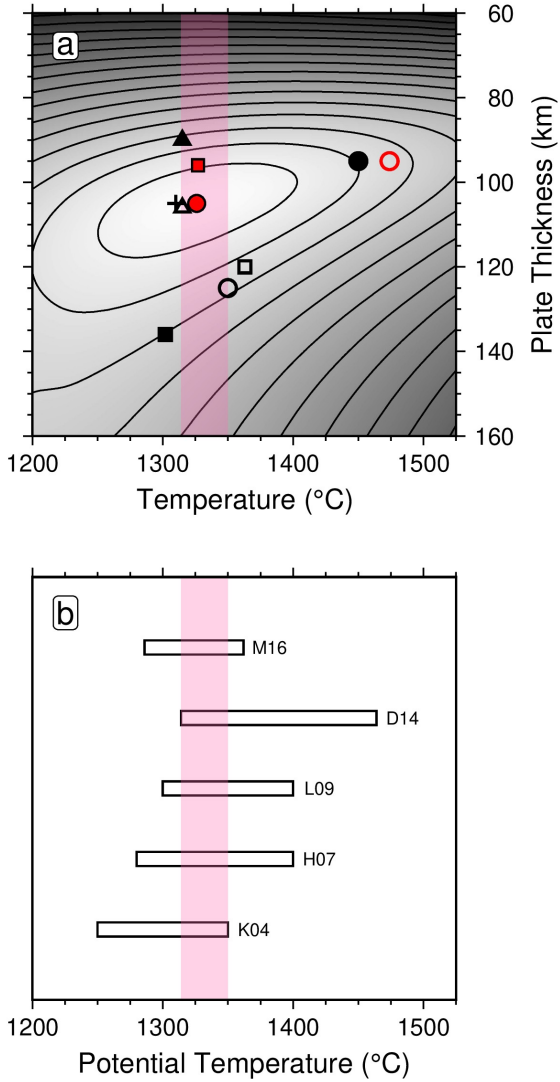


**Figure 8. Temperature and plate thickness estimates for range of reference models.** (a) Joint misfit between observed and calculated subsidence and heat flow plotted for revised analytical plate model HWR-2 as function of basal temperature and plate thickness (see Figure 5e). Open red circle = HWR-1 model ( $T_b = 1474 \pm 50^\circ\text{C}$ ;  $z_p = 95 \pm 10 \text{ km}$ ) ; filled red circle = HWR-2 model ( $T_b = 1326 \pm 50^\circ\text{C}$ ;  $z_p = 105 \pm 10 \text{ km}$ ); filled red square = HWR-3 model ( $T_p = 1326 \pm 50^\circ\text{C}$ ;  $z_p = 96 \pm 10 \text{ km}$ ); open black circle = Parsons and Sclater (1977) model ( $T_b = 1350 \pm 275^\circ\text{C}$ ;  $z_p = 125 \pm 10 \text{ km}$ ); filled black circle = Stein and Stein (1992) model ( $T_b = 1450 \pm 250^\circ\text{C}$ ;  $z_p = 95 \pm 15 \text{ km}$ ); black cross = CHABLIS model by Doin and Fleitout (1996) ( $T_m = 1310^\circ\text{C}$ ;  $z_p = 105 \text{ km}$ ); open black square = Hillier and Watts (2005) model ( $T_b = 1363 \pm 7^\circ\text{C}$ ;  $z_p = 120 \pm 21 \text{ km}$ ); open black triangle = McKenzie et al. (2005) model ( $T_p = 1315 \pm 6^\circ\text{C}$ ;  $z_p = 106 \text{ km}$ ) filled black triangle = Crosby et al. (2006) model ( $T_p = 1315 \pm 6^\circ\text{C}$ , adopted from McKenzie et al. (2005);  $z_p = 90 \text{ km}$ ); filled black square = Richards et al. (2018) ( $T_p = 1302 \pm 50^\circ\text{C}$ ;  $z_p = 136 \pm 30 \text{ km}$ ); vertical pink band = range which qualitatively honors the overlaps between independent petrologic/geochemical studies shown in panel (b) (i.e.,  $1314 \text{--} 1350^\circ\text{C}$ ). (b) Independent estimates of mantle temperature. K04 =  $1250 \text{--} 1350^\circ\text{C}$  (Katsura et al., 2004); H07 =  $1280 \text{--} 1400^\circ\text{C}$  (Herzberg et al., 2007); L09 =  $1350 \pm 50^\circ\text{C}$  (Lee et al., 2009); D14 =  $1314 \text{--} 1464^\circ\text{C}$  (Dalton et al., 2014); and M16 =  $1318^{+44}_{-32} \text{ }^\circ\text{C}$  (Matthews et al., 2016).

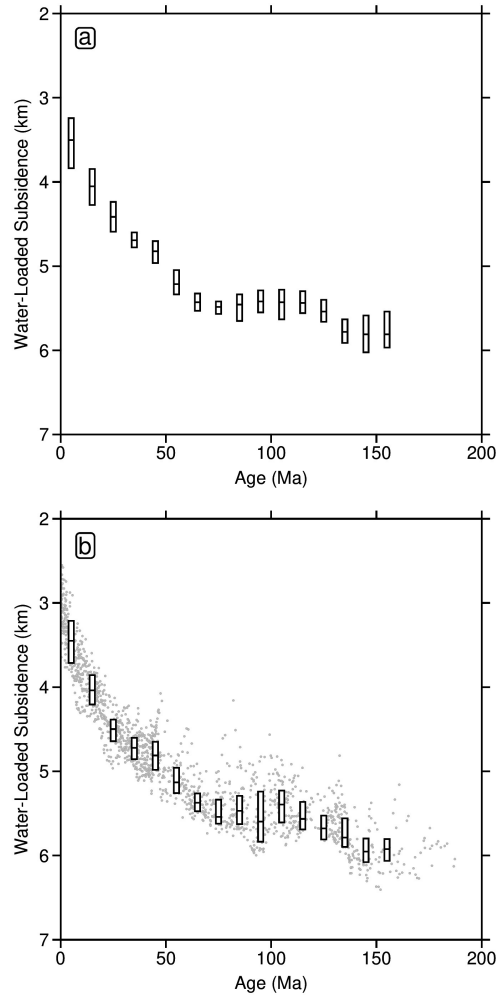


**Figure 9. Analysis of Crosby et al. (2006) observations.** (a) Age-depth measurements as function of oceanic plate age from portion of Pacific Ocean analyzed by Crosby et al. (2006). Horizontal bars with vertical gray boxes = median values with interquartile ranges of age-depth measurements binned every 10 Ma. Note plate shallowing centered on 100 Ma. (b) Age-depth measurements as function of oceanic plate age extracted from revised and augmented database of Holdt et al. (2022). Gray points = age-depth measurements from same portion of Pacific Ocean (see Pacific box of Figure 10 for location). Note that age-depth measurements are excluded in regions with anomalous topography and gravity, as identified by Crosby et al. (2006). Horizontal bars with vertical gray boxes = median values with interquartile ranges of age-depth measurements binned every 10 Ma. Note recovery of plate shallowing centered on 100 Ma.

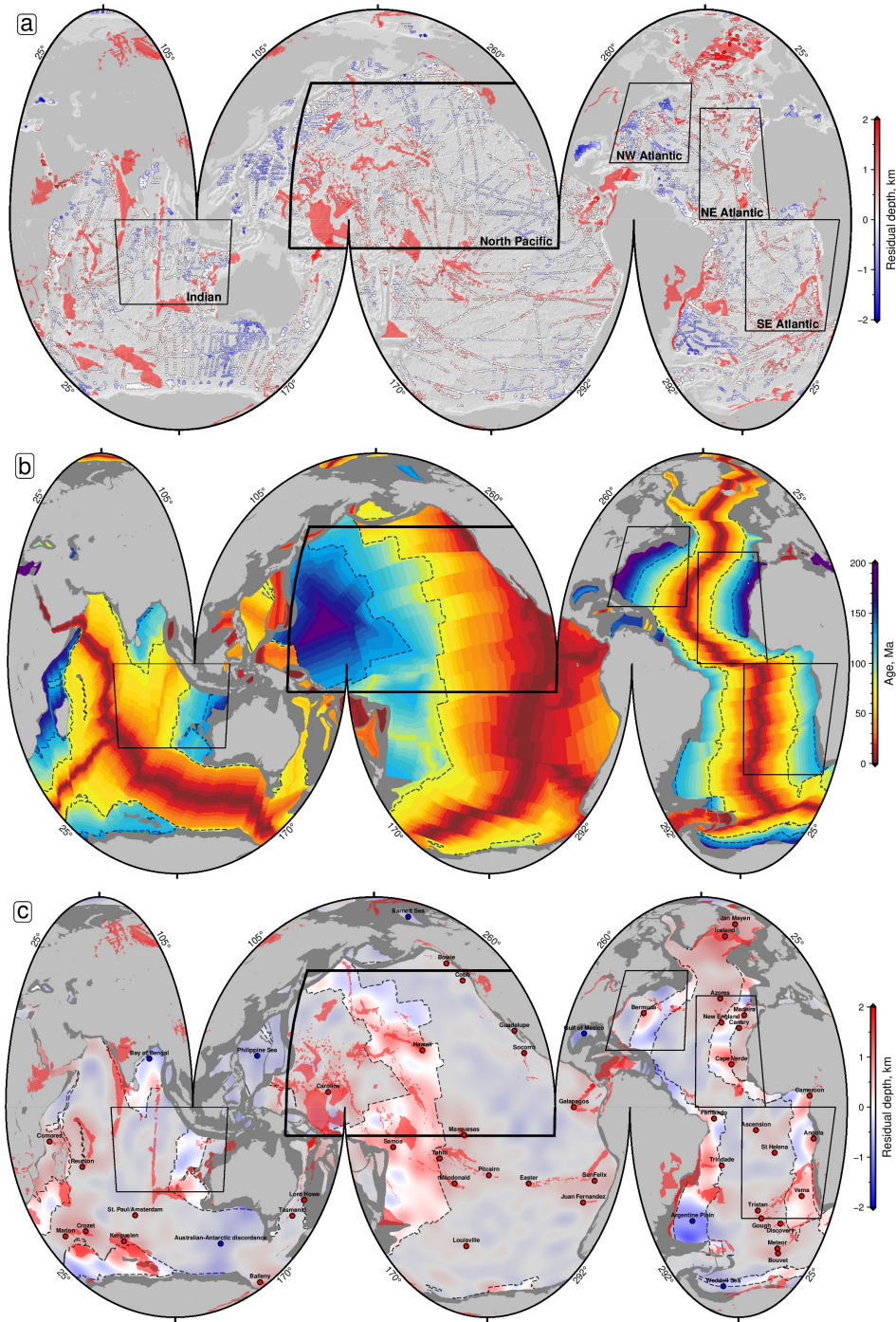


**Figure 10. Regions selected in plate model study of Crosby et al. (2006).** (a) Global distribution of residual depth measurements averaged over  $1^{\circ}$  bins. Circles = measurements with both sedimentary and crustal corrections; triangles = measurements for which only sedimentary corrections are applied. Red polygons = large igneous provinces and seamounts Coffin et al. (2006). Black box with thick outline = region of Pacific Ocean used to generate reference model by Crosby et al. (2006). Black boxes with thin outline = other regions where transient shallowing is observed by Crosby et al. (2006). (b) Augmented and revised age grid of Seton et al. (2020). Dashed contours = 80 and 130 Ma isochrons. (c) Spherical harmonic representation of residual depth measurements where  $l_{max} = 40$ . Transparent gray fill = oceanic crust  $< 80$  Ma and  $> 130$  Ma (i.e. region without transient shallowing observed by Crosby et al. (2006)). Red/blue circles = mantle plumes/drawdowns (see Supporting Information).

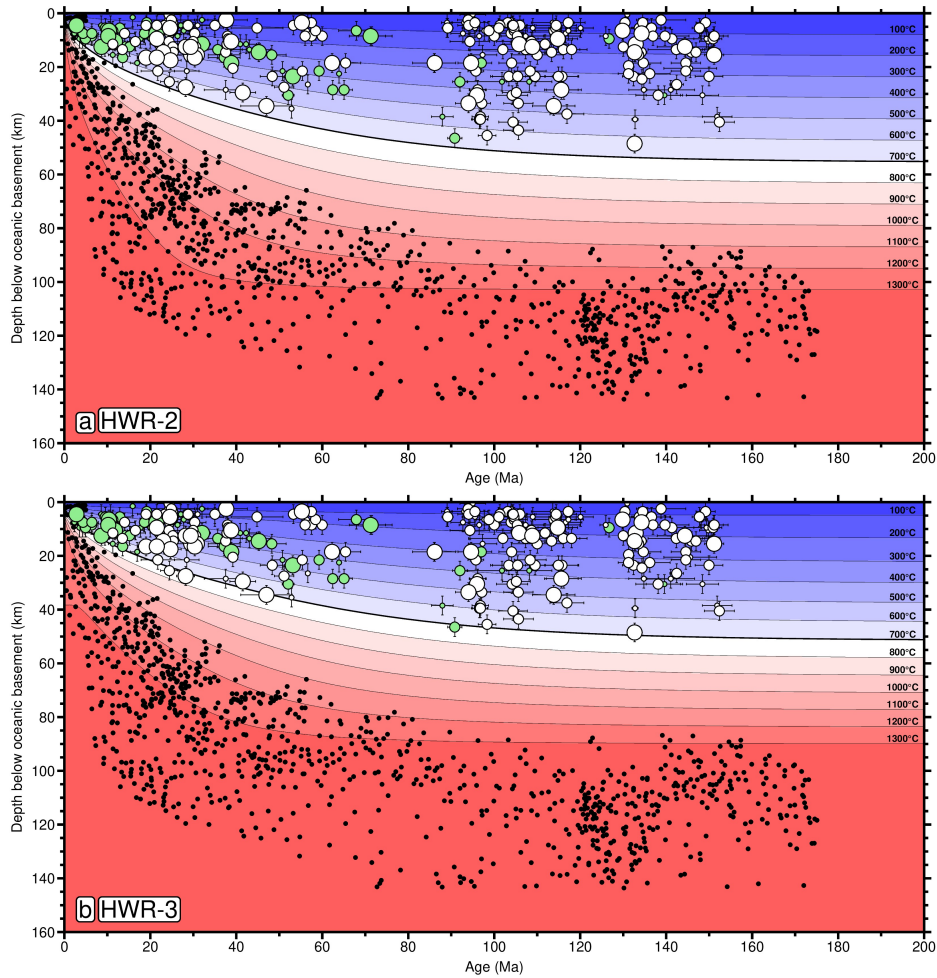


**Figure 11. Thermal structure of oceanic lithosphere.** (a) Thermal structure of oceanic lithosphere calculated using HWR-2 model. Contour lines = isothermal surfaces; green/white circles with errors = oceanic intraplate/outer rise earthquakes taken from Craig et al. (2014) where small, medium and large circles =  $M_b < 5.5$ , 5.5–6.5, and  $> 6.5$ ; bold contour line = 700°C isothermal surface, which identifies temperature above which oceanic earthquakes occur; solid black circles = measurements of depth to lithosphere-asthenosphere boundary zone determined from the orientation of azimuthal anisotropy,  $\psi_G$  (Burgos et al., 2014). (b) Same for HWR-3 model.

**674 Open Research Section**

675 Data files, code, and final models are available at Holdt et al. (2025). Residual depth  
676 measurements are published by Holdt et al. (2022), heat flow measurements are published  
677 by Hasterok et al. (2011), the age grid is published by Seton et al. (2020), earthquake  
678 depths are published by Craig et al. (2014) and azimuthal anisotropy measurements are  
679 published by Burgos et al. (2014).

**680 Acknowledgments**

681 MCH was supported by the Gates Cambridge Trust and by Project InnerSpace. We are  
682 grateful for G. Burgos and J.-P. Montanger for sending us their global azimuthal anisotropic  
683 measurements. We also thank H. Doran, A. Jackson and D. Lyness for their help. De-  
684 partment of Earth Sciences contribution number esc.120430.

685 **References**

- 686 Afonso, J. C., Ranalli, G., & Fernàndez, M. (2007). Density structure and buoyancy  
687 of the oceanic lithosphere revisited. *Geophysical Research Letters*, 34(10). doi:  
688 10.1029/2007GL029515
- 689 Berman, R. G., & Aranovich, L. Y. (1997). Optimized standard state and solu-  
690 tion properties of minerals I. Model calibration for olivine, orthopyroxene,  
691 cordierite, garnet, and ilmenite in the system FeO-MgO-CaO-Al<sub>2</sub>O<sub>3</sub>-TiO<sub>2</sub>-  
692 SiO<sub>2</sub>. *Contributions to Mineralogy and Petrology*, 126(1-2), 1-24. doi:  
693 10.1007/s004100050232
- 694 Boettcher, M. S., McGarr, A., Johnston, M., Jordan, T. H., Heesakkers, V., &  
695 Reches, Z. (2007). Constraints on Seismogenesis of Small Earthquakes (-2.8≤  
696 M W≤ 3) Defined by the Dense Instrument Network of the Natural Earth-  
697 quake Laboratory in South African Mines (NELSAM). In *Agu fall meeting  
698 abstracts* (Vol. 2007, pp. S33D-02).
- 699 Bouhifd, M. A., Andrault, D., Fiquet, G., & Richet, P. (1996). Thermal expansion of  
700 forsterite up to the melting point. *Geophysical Research Letters*, 23(10), 1143-  
701 1146. doi: 10.1029/96GL01118
- 702 Burgos, G., Montagner, J. P., Beucler, E., Capdeville, Y., Mocquet, A., & Drilleau,  
703 M. (2014). Oceanic lithosphere-asthenosphere boundary from surface wave  
704 dispersion data. *Journal of Geophysical Research: Solid Earth*, 119(2), 1079-  
705 1093. doi: 10.1002/2013JB010528
- 706 Carlson, R. L., & Jay Miller, D. (2004). Influence of pressure and mineralogy on  
707 seismic velocities in oceanic gabbros: Implications for the composition and  
708 state of the lower oceanic crust. *Journal of Geophysical Research: Solid Earth*,  
709 109(B9). doi: 10.1029/2003JB002699
- 710 Carslaw, H. S., & Jaeger, J. C. (1959). *Conduction of Heat in Solids*. (Second Edi-  
711 ed.). Oxford: Oxford University Press.
- 712 Christeson, G. L., Goff, J. A., & Reece, R. S. (2019). Synthesis of Oceanic Crustal  
713 Structure From Two-Dimensional Seismic Profiles. *Reviews of Geophysics*,  
714 57(2), 504-529. doi: 10.1029/2019RG000641
- 715 Coffin, M. F., Duncan, R. A., Eldholm, O., Fitton, J. G., Frey, F. A., Larsen, H. C.,  
716 ... Wallace, P. J. (2006). Large igneous provinces and scientific ocean  
717 drilling: Status quo and a look ahead. *Oceanography*, 19, 150-160. doi:  
718 10.5670/oceanog.2006.13
- 719 Coffin, M. F., & Eldholm, O. (1994). Large igneous provinces: Crustal structure, di-  
720 mensions, and external consequences. *Reviews of Geophysics*, 32(1), 1-36. doi:  
721 10.1029/93RG02508
- 722 Craig, T. J., Copley, A., & Jackson, J. (2014). A reassessment of outer-rise seis-  
723 micity and its implications for the mechanics of oceanic lithosphere. *Geophys-  
724 ical Journal International*, 197(1), 63-89. doi: 10.1093/gji/ggu013
- 725 Crosby, A. G., & McKenzie, D. P. (2009). An analysis of young ocean depth, grav-  
726 ity and global residual topography. *Geophysical Journal International*, 178(3),  
727 1198-1219. doi: 10.1111/j.1365-246X.2009.04224.x
- 728 Crosby, A. G., McKenzie, D. P., & Slater, J. G. (2006). The relationship between  
729 depth, age and gravity in the oceans. *Geophysical Journal International*,  
730 166(2), 553-573. doi: 10.1111/j.1365-246X.2006.03015.x
- 731 Dalton, C. A., Langmuir, C. H., & Gale, A. (2014). Geophysical and geochemical  
732 evidence for deep temperature variations beneath mid-ocean ridges. *Science*,  
733 344(6179), 80-83. doi: 10.1126/science.1249466
- 734 Davies, G. F. (1988). Ocean bathymetry and mantle convection. 2. Small-Scale  
735 Flow. *Journal of Geophysical Research*, 93(B9), 10,481-10,488. doi: 10.1029/  
736 jb093ib09p10467
- 737 Davis, E. E., & Lister, C. R. (1974). Fundamentals of ridge crest topogra-  
738 phy. *Earth and Planetary Science Letters*, 21(4), 405-413. doi: 10.1016/  
739 0012-821X(74)90180-0

- Dick, H. J. B., Natland, J. H., Alt, J. C., Bach, W., Bideau, D., Gee, J. S., ...  
 740  
 Holm, P. M. (2000). A long in situ section of the lower ocean crust: results  
 741 of ODP Leg 176 drilling at the Southwest Indian Ridge. *Earth and Planetary  
 742 Science Letters*, *179*(1), 31–51. doi: 10.1016/S0012-821X(00)00102-3  
 743
- Doin, M. P., & Fleitout, L. (1996). Thermal evolution of the oceanic lithosphere: An  
 744 alternative view. *Earth and Planetary Science Letters*, *142*(1-2), 121–136. doi:  
 745 10.1016/0012-821x(96)00082-9  
 746
- Galloway, W. E., Whiteaker, T. L., & Ganey-Curry, P. (2011). History of Ceno-  
 747 zoic North American drainage basin evolution, sediment yield, and accu-  
 748 mulation in the Gulf of Mexico basin. *Geosphere*, *7*(4), 938–973. doi:  
 749 10.1130/GES00647.1  
 750
- Goetze, C., & Evans, B. (1979). Stress and temperature in the bending lithosphere  
 751 as constrained by experimental rock mechanics. *Geophysical Journal Interna-  
 752 tional*, *59*(3), 463–478. doi: 10.1111/j.1365-246X.1979.tb02567.x  
 753
- Goranson, R. W. (1942). Heat capacity; Heat of fusion. In J. Birch, F. Schairer,  
 754 & H. Spicer (Eds.), *Handbook of physical constraints* (Vol. 36, pp. 223–242).  
 755 Boulder, Colorado: Geological Society of America, Special Paper. doi:  
 756 10.1130/SPE36-p223  
 757
- Goutorbe, B., & Hillier, J. K. (2013). An integration to optimally constrain the  
 758 thermal structure of oceanic lithosphere. *Journal of Geophysical Research: Solid  
 759 Earth*, *118*(1), 432–446. doi: 10.1029/2012JB009527  
 760
- Grose, C. J., & Afonso, J. C. (2013). Comprehensive plate models for the thermal  
 761 evolution of oceanic lithosphere. *Geochemistry, Geophysics, Geosystems*, *14*(9),  
 762 3751–3778. doi: 10.1002/ggge.20232  
 763
- Hasterok, D. (2013). Global patterns and vigor of ventilated hydrothermal circula-  
 764 tion through young seafloor. *Earth and Planetary Science Letters*, *380*, 12–20.  
 765 doi: 10.1016/j.epsl.2013.08.016  
 766
- Hasterok, D., Chapman, D. S., & Davis, E. E. (2011). Oceanic heat flow: Implica-  
 767 tions for global heat loss. *Earth and Planetary Science Letters*, *311*(3-4), 386–  
 768 395. doi: 10.1016/j.epsl.2011.09.044  
 769
- Herzberg, C., Asimow, P. D., Arndt, N., Niu, Y., Lesher, C. M., Fitton, J. G., ...  
 770  
 Saunders, A. D. (2007). Temperatures in ambient mantle and plumes: Con-  
 771 straints from basalts, picrites, and komatiites. *Geochemistry, Geophysics,  
 772 Geosystems*, *8*(2). doi: 10.1029/2006GC001390  
 773
- Hilde, T. W. C., Isezaki, N., & Wageman, J. M. (1976). Mesozoic Sea-Floor Spread-  
 774 ing in the North Pacific. *The geophysics of the Pacific Ocean basin and its  
 775 margin*, *19*, 205–226. doi: 10.1029/gm019p0205  
 776
- Hillier, J. K., & Watts, A. B. (2005). Relationship between depth and age in the  
 777 North Pacific Ocean. *Journal of Geophysical Research: Solid Earth*, *110*(2), 1–  
 778 22. doi: 10.1029/2004JB003406  
 779
- Hofmeister, A. M. (1999). Mantle values of thermal conductivity and the geotherm  
 780 from phonon lifetimes. *Science*, *283*(5408), 1699–1706. doi: 10.1126/science  
 781 .283.5408.1699  
 782
- Hofmeister, A. M. (2005). Dependence of diffusive radiative transfer on grain-size,  
 783 temperature, and Fe-content: Implications for mantle processes. *Journal of  
 784 Geodynamics*, *40*(1), 51–72. doi: 10.1016/j.jog.2005.06.001  
 785
- Hofmeister, A. M. (2007). Pressure dependence of thermal transport properties.  
 786 *Proceedings of the National Academy of Sciences of the United States of Amer-  
 787 ica*, *104*(22), 9192–9197. doi: 10.1073/pnas.0610734104  
 788
- Hofmeister, A. M. (2010). Thermal diffusivity of oxide perovskite compounds at el-  
 789 evated temperature. *Journal of Applied Physics*, *107*(10), 537–549. doi: 10  
 790 .1063/1.3371815  
 791
- Hoggard, M. J., White, N., & Al-Attar, D. (2016). Global dynamic topography  
 792 observations reveal limited influence of large-scale mantle flow. *Nature Geo-  
 793 science*, *9*(6), 456–463. doi: 10.1038/ngeo2709  
 794

- 795 Hoggard, M. J., Winterbourne, J., Czarnota, K., & White, N. (2017). Oceanic  
 796 residual depth measurements, the plate cooling model, and global dynamic  
 797 topography. *Journal of Geophysical Research: Solid Earth*, *122*(3), 2328–2372.  
 798 doi: 10.1002/2016JB013457
- 799 Holdt, M. C., White, N. J., Stephenson, S. N., & Conway-Jones, B. W. (2022).  
 800 Densely Sampled Global Dynamic Topographic Observations and Their Signif-  
 801 icance. *Journal of Geophysical Research: Solid Earth*, *127*(7), e2022JB024391.  
 802 doi: 10.1029/2022JB024391
- 803 Holdt, M., White, N., & Richards, F. (2025, January). *Supplementary material: "a*  
 804 *revised oceanic plate cooling model"*. Zenodo. Retrieved from <https://doi.org/10.5281/zenodo.14691107> doi: 10.5281/zenodo.14691107
- 805 Huang, J., & Zhong, S. (2005). Sublithospheric small-scale convection and its  
 806 implications for the residual topography at old ocean basins and the plate  
 807 model. *Journal of Geophysical Research: Solid Earth*, *110*(5), 1–17. doi:  
 808 10.1029/2004JB003153
- 809 Katsura, T., Yamada, H., Nishikawa, O., Song, M., Kubo, A., Shinmei, T., ... Fu-  
 810 nakoshi, K. (2004). Olivine-wadsleyite transition in the system (Mg,Fe)2  
 811 SiO4. *Journal of Geophysical Research: Solid Earth*, *109*(B02). doi:  
 812 10.1029/2003jb002438
- 813 Kelemen, P. B., Kikawa, E., Miller, D. J., & Party, S. S. (2004). *Shipboard Scientific*  
 814 *Party, Leg 209 Summary* (Vol. 209; Tech. Rep.). College Station, Texas.
- 815 Knapp, J. H., Knapp, C. C. D., Connor, J. A., McBride, J. H., & Simmons, M. D.  
 816 (2007). Deep seismic exploration of the South Caspian Basin: Lithosphere-  
 817 scale imaging of the world's deepest basin. In P. O. Yilmaz & G. H. Isaksen  
 818 (Eds.), *Oil and gas of the greater caspian area* (pp. 47–49). AAPG Special  
 819 Volumes. doi: 10.1306/1205831St553248
- 820 Korenaga, J. (2015). Seafloor topography and the thermal budget of Earth. *Ge-  
 821 ological Society of America Special Papers*, *514*, 167–185. doi: 10.1130/2015  
 822 .2514(11)
- 823 Korenaga, T., & Korenaga, J. (2016). Evolution of young oceanic lithosphere and  
 824 the meaning of seafloor subsidence rate. *Journal of Geophysical Research: Solid Earth*,  
 825 *121*(9), 6315–6332. doi: 10.1002/2016JB013395
- 826 Korenaga, T., Korenaga, J., Kawakatsu, H., & Yamano, M. (2021). A New  
 827 Reference Model for the Evolution of Oceanic Lithosphere in a Cooling  
 828 Earth. *Journal of Geophysical Research: Solid Earth*, *126*(6), 1–29. doi:  
 829 10.1029/2020JB021528
- 830 Larson, R. L., & Hilde, T. W. (1975). A revised time scale of magnetic reversals  
 831 for the Early Cretaceous and Late Jurassic. *Journal of Geophysical Research*,  
 832 *80*(17), 2586–2594. doi: 10.1029/JB080i017p02586
- 833 Lee, C. T. A., Luffi, P., Plank, T., Dalton, H., & Leeman, W. P. (2009). Con-  
 834 straints on the depths and temperatures of basaltic magma generation on  
 835 Earth and other terrestrial planets using new thermobarometers for mafic  
 836 magmas. *Earth and Planetary Science Letters*, *279*(1-2), 20–33. doi:  
 837 10.1016/j.epsl.2008.12.020
- 838 Matthews, S., Shorttle, O., & MacLennan, J. (2016). The temperature of  
 839 the Icelandic mantle from olivine-spinel aluminum exchange thermome-  
 840 try. *Geochemistry, Geophysics, Geosystems*, *17*(11), 4725–4752. doi:  
 841 10.1002/2016GC006497
- 842 McKenzie, D. P. (1967). Some remarks on heat flow and gravity anomalies. *Journal*  
 843 *of Geophysical Research*, *72*(24), 6261–6273. doi: 10.1029/jz072i024p06261
- 844 McKenzie, D. P., & Bickle, M. J. (1988). The volume and composition of melt gen-  
 845 erated by extension of the lithosphere. *Journal of Petrology*, *29*(3), 625–679.  
 846 doi: 10.1093/petrology/29.3.625
- 847 McKenzie, D. P., Jackson, J. A., & Priestley, K. (2005). Thermal structure of  
 848 oceanic and continental lithosphere. *Earth and Planetary Science Letters*,

- 233(3-4), 337–349. doi: 10.1016/j.epsl.2005.02.005
- Menard, H. W. (1973). Depth anomalies and the bobbing motion of drifting islands. *Journal of Geophysical Research*, 78(23), 5128–5137. doi: 10.1029/jb078i023p05128
- Parsons, B., & McKenzie, D. P. (1978). Mantle convection and the thermal structure of the plates. *Journal of Geophysical Research: Solid Earth*, 83(B9), 4485–4496. doi: 10.1029/JB083iB09p04485
- Parsons, B., & Sclater, J. G. (1977). An analysis of the variation of ocean floor bathymetry and heat flow with age. *Journal of Geophysical Research*, 82(5), 803–827. doi: 10.1029/jb082i005p00803
- Pertermann, M., & Hofmeister, A. M. (2006). Thermal diffusivity of olivine-group minerals at high temperature. *American Mineralogist*, 91(11-12), 1747–1760. doi: 10.2138/am.2006.2105
- Priestley, K., Ho, T., Takei, Y., & McKenzie, D. P. (2024). The thermal and anisotropic structure of the top 300 km of the mantle. *Earth and Planetary Science Letters*, 626, 118525. doi: 10.1016/j.epsl.2023.118525
- Priestley, K., & McKenzie, D. P. (2006). The thermal structure of the lithosphere from shear wave velocities. *Earth and Planetary Science Letters*, 244(1-2), 285–301. doi: 10.1016/j.epsl.2006.01.008
- Priestley, K., & McKenzie, D. P. (2013). The relationship between shear wave velocity, temperature, attenuation and viscosity in the shallow part of the mantle. *Earth and Planetary Science Letters*, 381, 78–91. doi: 10.1016/j.epsl.2013.08.022
- Richards, F. D., Hoggard, M., Crosby, A., Ghelichkhan, S., & White, N. (2020). Structure and dynamics of the oceanic lithosphere-asthenosphere system. *Physics of the Earth and Planetary Interiors*, 309(July), 106559. doi: 10.1016/j.pepi.2020.106559
- Richards, F. D., Hoggard, M. J., Cowton, L. R., & White, N. J. (2018). Reassessing the Thermal Structure of Oceanic Lithosphere With Revised Global Inventories of Basement Depths and Heat Flow Measurements. *Journal of Geophysical Research: Solid Earth*, 123(10), 9136–9161. doi: 10.1029/2018JB015998
- Rowley, D. B. (2019). Oceanic axial depth and age-depth distribution of oceanic lithosphere: Comparison of magnetic anomaly picks versus age-grid models. *Lithosphere*, 11(1), 21–43. doi: 10.1130/L1027.1
- Schatz, J. F., & Simmons, G. (1972). Thermal conductivity of Earth materials at high temperatures. *Journal of Geophysical Research*, 77(35), 6966–6983. doi: 10.1029/jb077i035p06966
- Sclater, J., Hasterok, D., Goutorbe, B., Hillier, J. K., & Negrete, R. (2014). Encyclopedia of Marine Geosciences. *Encyclopedia of Marine Geosciences*, 1–16. doi: 10.1007/978-94-007-6644-0
- Seton, M., Müller, R. D., Zahirovic, S., Williams, S., Wright, N. M., Cannon, J., ... McGirr, R. (2020). A Global Data Set of Present-Day Oceanic Crustal Age and Seafloor Spreading Parameters. *Geochemistry, Geophysics, Geosystems*, 21(10), 1–15. doi: 10.1029/2020GC009214
- Stein, C., & Stein, S. (1992). A model for the global variation in oceanic depth and heat flow with lithospheric age. *Nature*, 359(10), 123–129. doi: 10.1038/359123a0
- Steinberger, B., & Becker, T. W. (2018). A comparison of lithospheric thickness models. *Tectonophysics*, 746, 325–338. doi: 10.1016/j.tecto.2016.08.001
- Straume, E. O., Gaina, C., Medvedev, S., Hochmuth, K., Gohl, K., Whittaker, J. M., ... Hopper, J. R. (2019). GlobSed: Updated Total Sediment Thickness in the World's Oceans. *Geochemistry, Geophysics, Geosystems*, 20(4), 1756–1772. doi: 10.1029/2018GC008115
- Sydorenko, G., Stephenson, R., Yegorova, T., Starostenko, V., Tolkunov, A., Janik, T., ... Omelchenko, V. (2017). Geological structure of the northern part

- of the Eastern Black Sea from regional seismic reflection data including the DOBRE-2 CDP profile. In M. Sosson, R. Stephenson, & S. Adamia (Eds.), *Tectonic evolution of the eastern black sea and caucasus* (Vol. 428, pp. 307–321). London: Geological Society of London. doi: 10.1144/SP428.15
- Takeuchi, H., & Sakata, S. (1970). Convection in a mantle with variable viscosity. *Journal of Geophysical Research*, 75(5), 921–927. doi: 10.1029/jb075i005p00921
- Turcotte, D. L., & Oxburgh, E. R. (1967). Finite amplitude convective cells and continental drift. *Journal of Fluid Mechanics*, 28(1), 29–42. doi: 10.1017/S0022112067001880
- VanTongeren, J. A., Kelemen, P. B., Garrido, C. J., Godard, M., Hanghoj, K., Braun, M., & Pearce, J. A. (2021). The composition of the lower oceanic crust in the Wadi Khafifah section of the southern Samail (Oman) ophiolite. *Journal of Geophysical Research: Solid Earth*, 126(11), e2021JB021986. doi: 10.1029/2021JB021986
- Vogt, P. R., Anderson, C. N., & Bracey, D. R. (1971). Mesozoic magnetic anomalies, sea-floor spreading, and geomagnetic reversals in the southwestern North Atlantic. *Journal of Geophysical Research*, 76(20), 4796–4823. doi: 10.1029/jb076i020p04796
- Von Herzen, R. P., & Uyeda, S. (1963). Heat flow through the eastern Pacific ocean floor. *Journal of Geophysical Research*, 68(14), 4219–4250. doi: 10.1029/JZ068i014p04219
- Wessel, P., Sandwell, D. T., & Kim, S. S. (2010). The global seamount census. *Oceanography*, 23(1), 24–33. doi: 10.5670/oceanog.2010.60